# Rolled-up InGaAsP/InP Microtubes for Near-Infrared Integrated Lasers

Shouvik Mukherjee



Department of Electrical and Computer Engineering

Faculty of Engineering

McGill University

Montreal

A Thesis submitted to McGill University in partial fulfilment of the requirements towards the degree of Master of Engineering

Copyright © 2012 by Shouvik Mukherjee

To,

Bhagawan Sri Sathya Sai Baba

&

My Parents

## **ABSTRACT**

This thesis reports on the fabrication and characterization of rolled-up InGaAsP microtube lasers. The microtubes are created from an InGaAsP strained bilayer, grown on an InP substrate, with embedded InAs quantum dots and show strong resonant mode emission in the 1.5-1.6  $\mu$ m range at room temperature. The devices, operating under continuous wave optical pumping at 82K, show multimode lasing and an estimated ultra-low lasing threshold near 1.25  $\mu$ W optical power. These rolled-up microtube lasers show a great potential as integrated laser sources in silicon-based photonic circuits.

# **ABRÉGÉ**

Ce mémoire démontre la fabrication et la caractérisation de lasers fait de microtubes enroulés de InGaAsP. Les microtubes sont fabriqués à partir d'une bicouche sous tension d'InGaAsP sur un substrat de InP avec des points quantiques intégrés d'InAs qui montrent l'émission du mode résonant fort de l'ordre de 1,5-1,6 µm à température pièce. Le fonctionnement de ce laser ce fait sous pompage optique à 82K démontre une opération laser multi-modes possèdant un seuil estimé ultra-bas du laser près de 1,25 µW de la puissance optique absorbée. Ces microtubes enroulés démontrent un grand potentiel en tant que source de laser intéré dans des circuits photoniques à base de silicium.

#### **ACKNOWLEDGEMENT**

This master's thesis could not have been finished without the supervision, support and encouragement from my peers, colleagues, family and friends. The author wishes to express his sincere appreciation to those who involved in his work in this dissertation.

First of all, I would like to convey heartfelt gratitude to my senior supervisor Professor Zetian Mi for offering me an opportunity to study and learn under his able guidance by being a part of a dynamic research group in McGill University. His supervision has not only been instrumental in honing my research capabilities but has also trained me extensively in the field of academics for pursuing my future career prospects.

I would also like to thank my co-supervisor Dr. Pablo Bianucci for his continuous guidance and instructive support. Under his tutelage, I gained experience in handling and working with optical instruments and am deeply thankful for his suggestions, and valuation of my research topics.

Last but never the least; I would like to thank my parents, Shrabani Mukherjee and Prosit Mukherjee and my guide and well-wisher Bhagawan Sri Sathya Sai Baba for their love, encouragement and belief in me.

This work is supported by the Natural Sciences and Engineering Research Council of Canada (NSERC), the Fonds de recherché sur la nature et les technologies, Canada Foundation for Innovation, and the Hydro-Quebec Nano-Engineering Program at McGill University.

# TABLE OF CONTENTS

DEDICATIONii
ABSTRACTiii
ABRÉGÉiv
ACKNOWLEDGEMENTv
LIST OF FIGURESix
LIST OF APPENDICESxii
CHAPTER
1.Introduction1
1.1 Overview
1.2 Optical Interconnects
1.3 Light Emission in Microcavities4
1.4 Rolled-Up Microtube (RUMT) Structures5
1.5 Thesis Organisation5
2. Background
2.1 Basics of Lasers
2.2 Semiconductor Lasers9
2.3 Nanostructured Semiconductor Gain Media9
2.4 Semiconductor Quantum Dots
2.5 Band Structure of Quantum Dots
2.6 Essentials of Optical Microcavities
2.6.1 Optical Confinement in Microcavities
2.6.2 Fabry Perot Resonator
2.6.3 Free Spectral Range

	2.6.4	Quality Factor	16
	2.6.5	Finesse	18
	2.6.6	Field Enhancement	18
	2.7 Quantum	Dot in Microcavities	19
	2.7.1	Purcell Effect	19
	2.7.2	Spontaneous Emission Factor	20
3. F	abrication		21
	3.1 Rolling in	Strained Nano Membranes	22
	3.2 Layered H	Heterostructure	25
	3.3 Fabricatio	on of InGaAsP Microtubes	26
4. Photoluminescence Studies28			
	4.1 Photolumin	nescence	28
	4.2 Experiment	tal Setup	28
	4.3 PL Spectro	scopy of InGaAsP Microtubes	30
	4.4 Modelling		
		Microtubes as Optical Cavities	32
		Microtubes as Optical Cavities	
	4.5 Discussion		34
	<ul><li>4.5 Discussion</li><li>4.6 Optical Fie</li></ul>		34 36
5. R	<ul><li>4.5 Discussion</li><li>4.6 Optical Field</li><li>4.7 Finite Difference</li></ul>	ld Distribution	34
5. R	4.5 Discussion 4.6 Optical Fiel 4.7 Finite Diffeolled-up InGaA	ld Distributionerence Time Domain (FDTD) Simulation Results	34 36 39
5. R	4.5 Discussion 4.6 Optical Fiel 4.7 Finite Diffe  olled-up InGaA  5.1 Introduction	ld Distributionerence Time Domain (FDTD) Simulation Results	34363941

Appendix I:	48
Appendix II:	51
Bibliography	55

# LIST OF FIGURES

# **Figure**

1.	Thin film micro-lasers for intra-chip optical interconnects
2.	5 basic components of a laser; 1- Active gain medium, 2-Laser pumping
	energy, 3- High reflector, 4-Output coupler (which together with the high
	reflector forms the optical cavity), 5- Collimated laser beam
3.	Stranski-Krastanow growth mechanism of InAs quantum dots on GaAs 12
4.	A Fabry-Perot Cavity with an illustration of the paths of light inside it 15
5.	Transmission and Reflection peaks inside a Fabry-Perot cavity. Variation in
	mode linewidth due to variation in Finesse from 2 (blue) to 10 (red) 16
6.	Lorentzian approximation to the energy distribution of the mode peak
	illustrating Q factor in terms of resonance frequency $f_0$ and FWHM $\Delta f_{\dots}$ . 17
7.	Illustration of the formation mechanism of strain-induced self-rolling of a
	semiconductor nanotube from a rectangle stripe, illustrated with InAs/GaAs
	bilayer and AlAs sacrificial layer
8.	a) U-shaped InGaAsP mesa definition. b) Post-rolling microtube with free-
	standing section
9	Schematic of InGaAsP/InP Layered Structure 25

10.	a) Free-standing InGaAsP rolled-up microtube. b) SEM image illustrating
	periodic corrugations along the sides of the tube. c) SEM image illustrating
	the number of turns in a particular device-3
11.	Schematic of PL setup used and its components
12.	PL spectra for the as-grown sample (dashed line) and a rolled, non-free-
	standing microtube (solid line) measured at room temperature 30
13.	Rolled-up Microtube (RUMT) PL emission from free standing region or
	two turn sample. The mode azimuthal number is denoted by (m) 31
14.	Microtube bottle resonator illustrating light propagation due to effective
	wave guiding (red)
15.	Cross-section of a microtube showing the two sections with different wall
	thicknesses and the inner and outer notches
16.	Complete resonance spectrum of InP microtube computed from the quasi-
	Schrödinger wave equation
17.	Rolled-up Microtube (RUMT) PL emission from free standing region of
	two turn (top) and one turn (below) samples. The mode azimuthal and axia
	mode numbers are denoted in the order (m,p)
18.	TE polarized distribution with electric field parallel to tube axis and TM
	polarization normal to the tube wall
19.	a) Electric field distribution of a 2-turn 84 nm thick tube wall, with
	azimuthal wave number m=16 at resonant wavelength 1463 nm. The inner
	notch characterizes the directional nature of the emission. b) Electric field

	distribution for a 3-turn 126 nm thick tube wall, with m=22 at resonant
	wavelength 1440 nm showing better directional emission due to presence of
	inner notch. The notch is indicated by the arrow (in both cases)
20.	a) Photoluminescence spectra of an InGaAsP microtube at 5.6 $\mu W$ (black)
	and 180 nW (red) under low temperature (82 K) conditions. The dashed
	curve represents the spectrum of an as-grown sample under same conditions
	and the box illustrates a point 8 nm away from the mode to obtain
	background emission characteristics. b) Evolutions of spectra of modes
	(22,1) and (22,4) with increasing absorbed pump power
21.	a) Peak integrated area curve for mode (22,1) and the emission from the
	background (green) vs. Pump Power. Lower Inset: FWHM of the (22,1)
	mode illustrating abrupt decrease after threshold to confirm lasing. Upper
	Inset: Peak area vs Pump power intensity plot in Log scale clearly showing
	threshold. b) a) Peak integrated area curve for mode (22,4) indicating no
	significant decrease in peak linewidth at high powers

# LIST OF APPENDICES

APPENDIX I	48
APPENDIX II	51

## Chapter I

## Introduction

#### 1.1 Overview

With the advent of the digital age, the need to design and incorporate smaller and highly precise computing components has grown exponentially. The future holds promise in incorporating both electronic and photonic device components to achieve this common goal. The continuing exponential reduction in feature sizes on electronic chips, as governed by Moore's Law [1], has prompted the need for developing larger number of faster devices operating at lower cost per device. Conventional electronic interconnections are rapidly becoming a roadblock to the continued application of Moore's law. One of the predominant approaches to solving this issue is changing the physical media responsible for interconnect operations, i.e. using light instead of electrons. Optical interconnects could solve many physical problems of interconnects such as precise clock distribution, system synchronization, bandwidth and density of long interconnections, and reduction of power dissipation.

Because of their small size and integration capability, microscale lasers are perfectly suited as light sources in optical interconnects. A microscale laser is formed when an optical gain medium is put within an optical microcavity. An optical gain medium amplifies light by means of stimulated emission, while an optical microcavity is a structure where light can be confined both spatially and temporally at the microscale. In lasers and other optical devices, these

cavities generally cause a standing wave to from inside the active optical medium.

Optical microcavity devices have become essential largely in part due to their highly efficient light confinement abilities in small scale volumes. Because of the confinement of light's electromagnetic field, several effects can be observed (enhancement of the confined field, modifications of the medium's spontaneous emission rate, less active media required for lasing etc.). The small size factor is thus instrumental in ensuring faster operation speed, lower power consumptions and higher integration density.

High-performing micro- and nano-scale optical devices are critical in forming digital optical communication links and on-chip optical interconnects between computing devices. We first briefly look at the evolution of optical interconnects and the role of micro- and nano-scale optical microcavities in future chip level integrations.

## **1.2 Optical Interconnects**

The evolution and need for optical interconnects is best understood by examining the current status and future requirements in the telecommunication and computing systems fields. Within a computer, tiny aluminium and copper interconnects [2] have traditionally provided the necessary connections required for efficient data transfer. However, with the advancements in computer processing speeds, more and more data needs to be manipulated at a faster rate. Growing concerns regarding power consumption, cross-talk, distortion and pin-out capacity have prompted physicists and engineers to turn to alternative solutions for inter-chip signalling. Moreover, fundamental

quantum effect limit the miniaturization and transfer rate in the metal interconnects.

Optical interconnects have a significant advantage over conventional electrical ones, offering higher bandwidth in the order of tens of GHz of data transfer rate (demonstrated with quantum dot lasers), as well being crosstalk-free, with inherent parallel processing and lower power dissipation [3, 4]. System level applications of these devices use several interconnect techniques such as free space, guided wave, wave, board-level and fiber array interconnections.

A possible approach for a compact intra-chip optical link is the use of a Silicon-on-Insulator (SOI) passive waveguide layer in combination with III-V semiconductor microlasers and micro-photodetectors, which are defined in a III-V membrane bonded on top of the SOI-stack (Figure 1), as demonstrated by Liu *et al* [5].

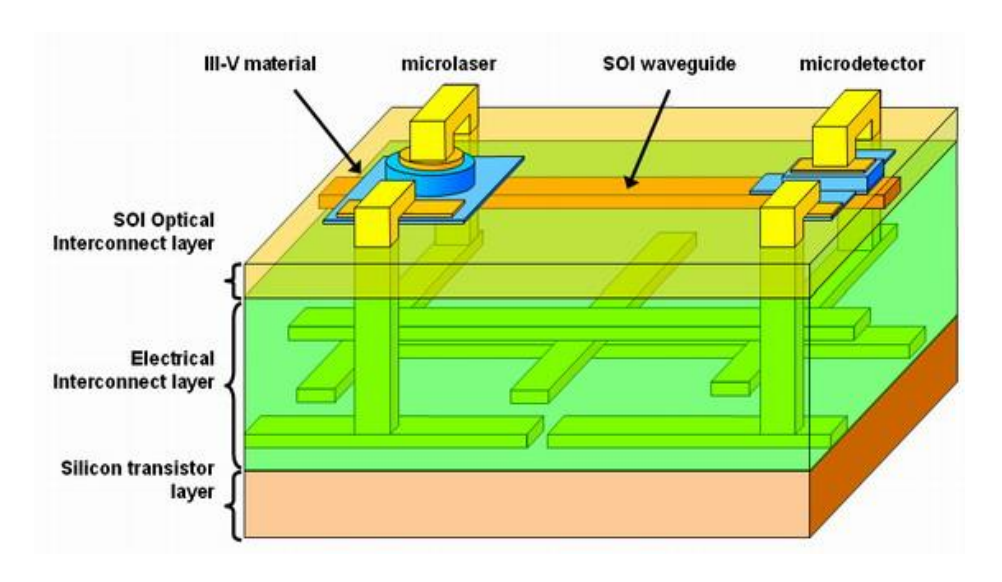


Figure 1: Thin film micro-lasers for intra-chip optical interconnects [5]

While these solutions are attractive in due to their high bandwidth capacity and simple architectural design, a cost-effective practical implementation remains a far off goal. In particular, concerns regarding effective light guiding/steering, scattering, and effective packaging structure remain largely in the research field.

The high performance of quantum-dot emitters and microcavity waveguides has encouraged research onto their selective growth and discrete transfer onto silicon [3, 4], with microtubes representing a strong prospect for continuous operation at low and room temperatures.

#### 1.3 Light Emission in Microcavities

To begin the discussion about the optical characteristics of microcavities, let us briefly examine the behaviour of light in a generic optical resonator. An optical resonator consists of reflective elements, arranged in a specific manner which supports a standing wave pattern of light due to the constructive interference of multiple reflections. These standing wave patterns only appear at certain wavelengths or frequencies, each one with a particular spatial pattern know as a resonant mode.

When the characteristic dimensions of the optical resonator are microscopic, it is referred to as an optical microcavity. Because of their small volume light can be confined more strongly within them. These structures then allow for a higher degree of control of the optical emission properties of materials placed inside them. They can, for example, modify the spatial distribution of radiated power, change the spectral width of the emitted light, and enhance or suppress the spontaneous emission rate. With the advancement of fabrication technology, these structures have not only been produced but have also attracted attention for lasers. Optical microcavities open the possibility of ultra-small lasers with low power consumption, and have potential for threshold-less lasing operation owing to the high efficiency coupling of

spontaneous emission into a single lasing mode, to name a few of the reasons that warrant this attention.

There have been many different types of microcavities studied in recent years. A small sample of these includes structures like microdisks, microcoils, micropillars, photonic crystals and nanowires [6-9]. For applications in lasers, active materials such as quantum wells and quantum dots are often used as light emitters.

## 1.4 Rolled-Up Microtube Structures (RUMTs)

Rolled-up microtube structures (RUMTs) are another type of optical microresonator that have recently become widely investigated, showing promise in the field of micro- and nano-optical devices. First successfully fabricated by Prinze *et al* in 2000 [7]; RUMTs are three-dimensional tubes fabricated from strained layers, combining traditional top-down fabrication processes with a bottom-up self-rolling mechanism for tube formation.

RUMTs exhibit very interesting optical properties owing to their unique tubular structure and associated degrees of freedom that allow for precise engineering of the resonant mode properties and can be used as laser sources and microfluidic sensors, among other applications.

## 1.5 Thesis Organization

This thesis focuses on the development and characterization of novel InGaAsP rolled-up microtube structures for lasing applications in integrated optical communications and will be organised as follows.

Chapter 2 discusses some key background concepts associated with semiconductor microtube structures. We start by looking at recent trends in semiconductor optoelectronic devices and the active media being used in these structures. This will be followed by a more detailed description of optical microcavities. We then discuss typically used nanostructured emission sources (in particular quantum dots and their properties), as well as rolled-up microtube structures and some basic concepts associated with lasing.

In Chapter 3, the fabrication technique of these structures is discussed. We shall first look at the layered InGaAsP structures used to fabricate the devices. Further discussions involving the self-rolling mechanism (which leads to tube formation), mesa orientation and rolling edge engineering will be explored.

Chapter 4 explores the photoluminescence (PL) studies performed on the devices described in chapter 3. We shall see a brief description of the experimental PL setup and its key components, and detailed discussion of the measured PL spectra. The chapter also explores the modelling of the optical modes in the microtubes using an equivalent planar waveguide model which provides insight into the factor which govern the optical properties.

Chapter 5 presents the achievement of an InGaAsP microtube laser at cryogenic temperatures (82 K) using InAs quantum dots as the active medium. Detailed spectroscopy and power dependent measurements are shown which demonstrate the lasing phenomenon. Finally, a brief conclusion and suggestions for future work are outlined.

## **Chapter II**

# **Background**

#### 2.1 Basics of Lasers

Lasers are essentially coherent light sources comprising of several components which work together to achieve light amplification by the process of stimulated emission. A schematic laser and its components are illustrated in Figure 2. In this section, we shall look at the three most critical components, namely the active gain medium, the laser pump source and the resonant optical cavity.

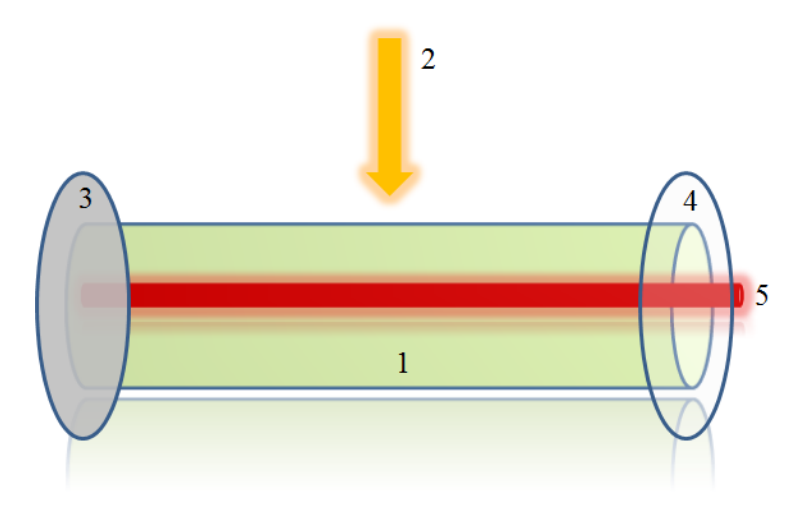


Figure 2: 5 basic components of a laser; 1- Active gain medium, 2-Laser pumping energy, 3- High reflector, 4-Output coupler (which together with the high reflector forms the optical cavity), 5-Collimated laser beam

The basic operation of a laser is summarized as follows: The atoms in the gain medium can interact with light both by absorbing and by emitting photons. When the gain medium absorbs pump energy, some electrons in their constituent atoms are raised from their lowest energy ("ground") states into higher-energy ("excited") quantum states These excited atomic states can emit

photons, with the emission being either spontaneous or stimulated. Spontaneous emission is isotropic and independent of any light that might be present within the medium, while stimulated emission depends on the photons present in the medium and is emitted with the same direction and phase as the stimulating light. When the number of atoms in the excited state exceeds the number of atoms in the ground state, population inversion is achieved and the amount of stimulated emission due to light that passes through the medium is larger than the amount of absorption. Hence, the light within the medium is amplified. By itself, this makes an optical amplifier. When this amplifying medium is put into a resonant optical cavity, which provides optical feedback, the result is a laser.

When the active medium is pumped above inversion, an initial photon that is emitted (usually by spontaneous emission) will trigger the stimulated emission of more photons. Thanks to the optical feedback provided by the cavity, these photons will stimulate further emission and a cascade of stimulated emission occurs, giving rise to lasing. The light generated by stimulated emission is identical to the input signal in terms of wavelength, phase, and polarization. This gives laser light its characteristic coherence, and allows it to maintain the uniform polarization and often quasi-monochromatic behavior established by the optical cavity design. In the following sections, we shall be focusing on semiconductor lasers and in particular rolled-up microtube lasers and their tunability aspects.

#### 2.2 Semiconductor Lasers

Semiconductor lasers use semiconductor gain media. Similar to what was described in the previous section; here optical gain is usually achieved by stimulated emission at an inter-band transition under conditions of a high carrier density in the conduction and valence bands. As such, the excited stateground state transition takes place between the conduction and valence band respectively of the semiconductor material. Thus, the bandgap of the semiconductor plays a crucial role in determining the onset/threshold of lasing and as we shall see in subsequent sections, determines the tunability of the device to emit light at a specific wavelength. The road to achieving population inversion and stimulated emission is also governed by the bandgap of the material. Optical pump sources (usually lasers) are used to produce a photon beam with energy slightly larger than the bandgap of the material and thus excite the electrons from the valence to the conduction band. It is also possible to inject carriers through electrical contacts. Conventionally, direct bandgap materials such as III-V semiconductors (GaAs, GaP, InP, InAs, and alloys) have been used as gain material in bulk or nanostructured form, displaying a stronger and more efficient light emission than indirect bandgap materials such as silicon and germanium.

#### 2.3 Nanostructured semiconductor gain media

In recent times, semiconductor nanostructures, such as quantum wells (QD) and quantum dots (QD) have been explored as active gain media for semiconductor lasers. The use of nanostructures instead of bulk media enhances laser performance. Besides enhanced performance, nanostructures

allow for tuning of the inter-band transition and give a high degree of tunability to semiconductor lasers.

In addition to the wavelength tunability, quantum confinement comes into play when one or more dimensions of a semiconductor nanostructure approach the Bohr radius limit of an electron-hole pair (exciton). In this case, the electronic density of states (DOS) is modified, resulting in highly-enhanced transition probabilities.

Quantum well systems consist of a very thin (less than the exciton Bohr radius) active layer with higher-bandgap material surrounding it. Excitons created in the well are then confined to a two dimensional state. Due to the flexibility in the material choices, a large spectrum of laser emission is unlocked by quantum wells. For instance, strained QW lasers have been demonstrated near the 0.7-0.8 μm range and near-infrared 0.9-1.2 μm range using InGaAs/GaAs heterostructures [10] Devices have also been demonstrated in the telecommunication wavelength region of 1.3-1.55 μm using InGaAsP structures.

On the whole, there are thus a number of advantages of lasers using nanoscale emission sources such as quantum wells and quantum dots, over conventional bulk media. The confinement and resultant enhanced density of states gives us the ability to "tune" the resultant wavelength of the device. This is achieved by changing the length of one of the dimensions of a quantum well or quantum dot. Moreover, lower threshold carrier density is achievable by changing the overall thickness of the active layer, a feat which is hard to induce in bulk semiconductor lasers.

## 2.4 Semiconductor Quantum Dots

Quantum dots are small islands of a lower bandgap semiconductor surrounded by a higher bandgap one. When these islands are small enough excitons created inside are confined in all three spatial dimensions. Their size (~ 2- 40 nm) is crucial in determining their properties which fall somewhere between bulk semiconductors and discrete molecules. The high level of control over the size of these crystals gives us control over the optical properties of the material. Moreover, high-quality quantum dots are well suited for optical encoding and multiplexing applications due to their broad excitation profiles and narrow/symmetric emission spectra.

Self-organized quantum dots are grown using the Stranski-Krastanow growth method [11, 12]. Typically, both molecular beam epitaxy (MBE) and metal organic chemical vapor deposition (MOCVD) methods have been used to grow self-organised quantum dots. This method involves growing a material layer (for e.g. InAs) on a substrate (e.g. GaAs) with an inherent mismatch between their crystal lattice constants in the range of ~ 1.8% or larger. This coherent strain results in the development of small islands of material on top of a two dimensional "wetting" layer. These islands are then subsequently buried to form quantum dots. Figure 3 illustrates the Stranski-Krastanow growth process.

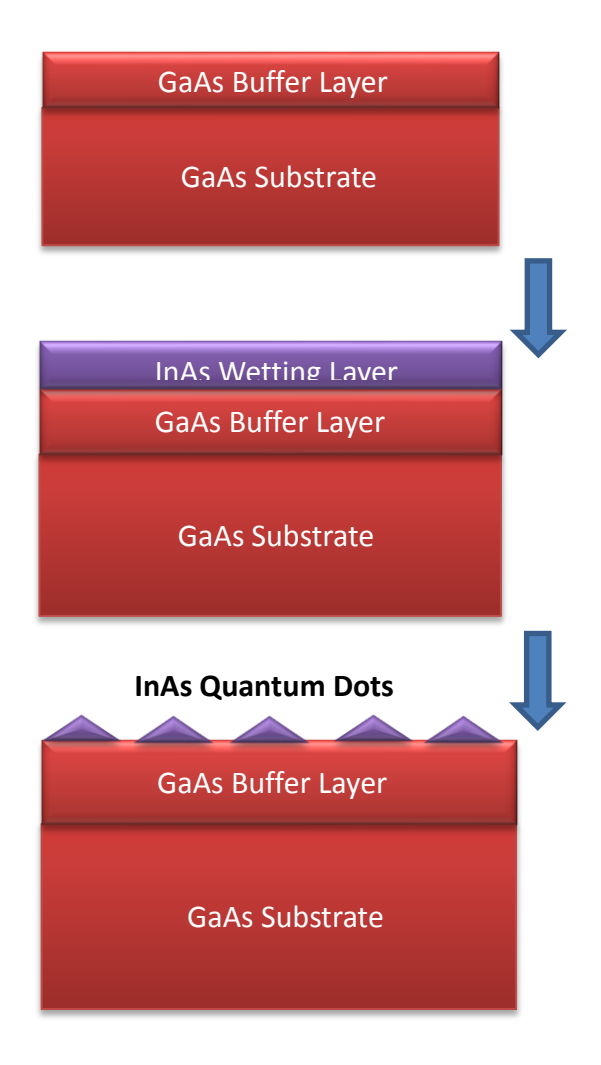


Figure 3: Stranski-Krastanow growth mechanism of InAs quantum dots on GaAs.

## 2.5 Band Structure of Quantum Dots

It is possible to use a simplified particle-in-a-box effective-mass model [13]to understand the energy structure of quantum dots. We find that the bandgap energy that determines the energy (and hence wavelength) of the emitted light is inversely proportional to the size of the quantum dot.

Thus, the smaller the quantum dot, the wider the band gap. The band gap of GaAs in bulk, for example, is 1.52 eV, while a 94 nm thick quantum dot layer of arsenic has a band gap of 2.8 eV, and a dot layer half as big (47 nm), has a band gap of 3.2 eV, about twice that of the bulk material [14].

Because of quantum confinement, quantum dots possess discrete electron and hole energy levels (which can also be studied using the particle-in-a-box model). As a consequence, optical absorption and emission occur at discrete energies which are determined by the size and the shape of the dot. Thus the lifetime and wavelength of emission also depends upon the size of the dot [15]. At low excitation density, light emission is due to decay of the lowest exciton state to the ground state. At higher excitation densities, light emission from higher-energy excitonic states can become apparent. In the same vein, quantum dot absorption shows peaks corresponding to the excitonic states. It is worth noting that larger quantum dots have more energy levels which are also more closely spaced, allowing for the presence of more excitonic excited states.

## 2.6 Essentials of Optical Microcavities

We saw in the last section a qualitative description of the gain media used in our semiconductor rolled-up microtube lasers. In this section we shall examine the optical cavity structure that supports the emission of these quantum dots.

## **2.6.1 Optical Confinement in Microcavities**

An optical cavity or an optical resonator in general, is an arrangement of optical components, which allows a beam of light to circulate in a closed path. Optical microcavities are structures that enable confinement of light to micro-scale volumes. This confinement effect is achieved by resonant recirculation. The modes (chapter 4) correspond to the wavelengths of the light wave which are reinforced by constructive interference after many reflections from the cavity's reflecting surfaces. All other wavelengths are suppressed by

destructive interference. An ideal cavity would confine light in definitely (that is, without loss) and would have resonant frequencies at precise values. The presence of losses causes some degree of broadening at the resonance frequency.

The key difference between microcavities and regular optical cavities are observed under the dimensional limitations of the former. Micro-scale volume ensures that the field is more tightly confined and enhanced respect to that of a macro-scale resonator. Besides, resonant frequencies are more sparsely distributed throughout this spectrum in a micro-scale resonator than they are in a corresponding macro-scale one.

## 2.6.2 Fabry Perot Resonator

Some of the key optical parameters associated with the degree of confinement in an optical cavity are best described by looking at one of the most well-known optical resonator structures. A simple device that relies on the interference of multiple beams, the Fabry-Perot cavity [16] consists of two partially transmitting mirrors precisely aligned to form a reflective cavity. Incident light enters the Fabry-Perot cavity and undergoes multiple reflections between the mirrors so that the light interferes with itself many times (Figure 4) leading to constructive and destructive interferences.

If the frequency of the incident light is such that constructive interference occurs within the Fabry-Perot cavity, the light will be transmitted. Otherwise, destructive interference will not allow any light through the Fabry-Perot cavity.

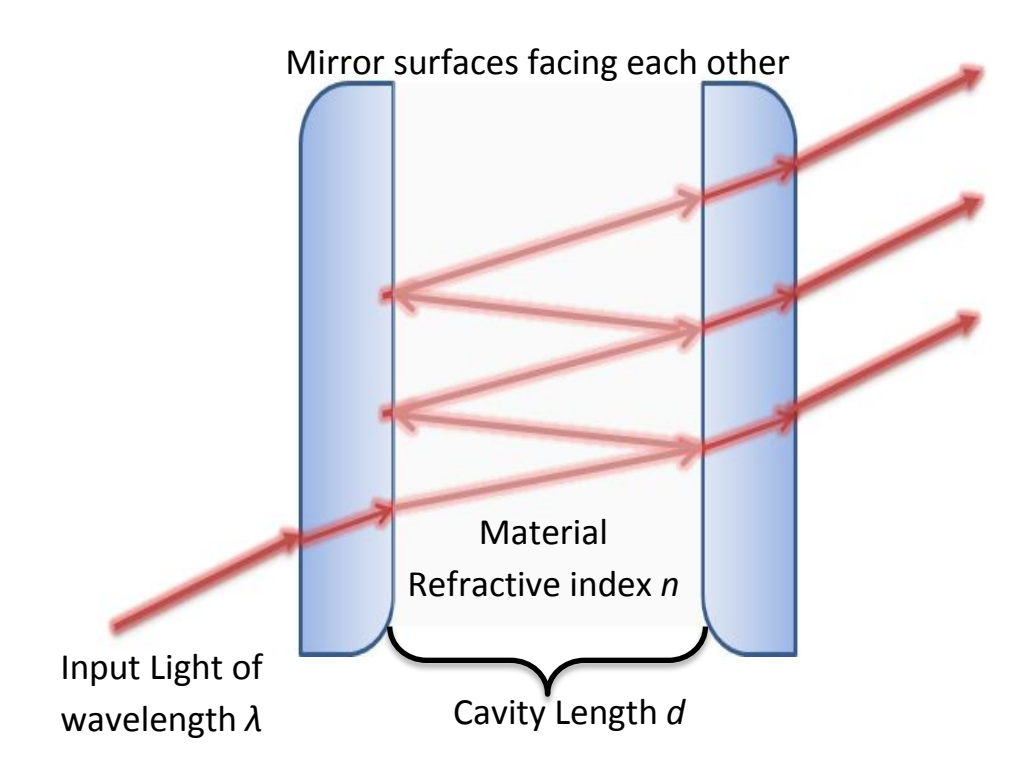


Figure 4: A Fabry-Perot Cavity with an illustration of the paths of light inside it.

Constructive interference between multiple reflections results in transmission peaks as can be seen in Figure 5. These are the resonant modes of the optical cavity. In subsequent sections we look at some key parameters associated with the transmission peaks or modes, namely: the free spectral range (FSR), the full width at half maximum (FWHM), the mode volume, the quality factor and the finesse.

While the Fabry-Perot cavity confers longitudinal confinement of light, perpendicular confinement and other such aspects are induced by the geometry and other properties of the structure. These dependencies shall be examined in chapter 4.

## 2.6.3 Free Spectral Range

The free spectral range (FSR) given by  $\Delta\lambda$  (Figure 5) denotes the spacing between adjacent resonances. Using a generalized formula [17],  $\Delta\lambda \approx \frac{\lambda^2}{2nd}$ , we see that it depends upon central wavelength of emission  $\lambda$ , the refractive index of the material between the mirrors n ( n=1 for air) and the length of the cavity itself d (Figure 4).

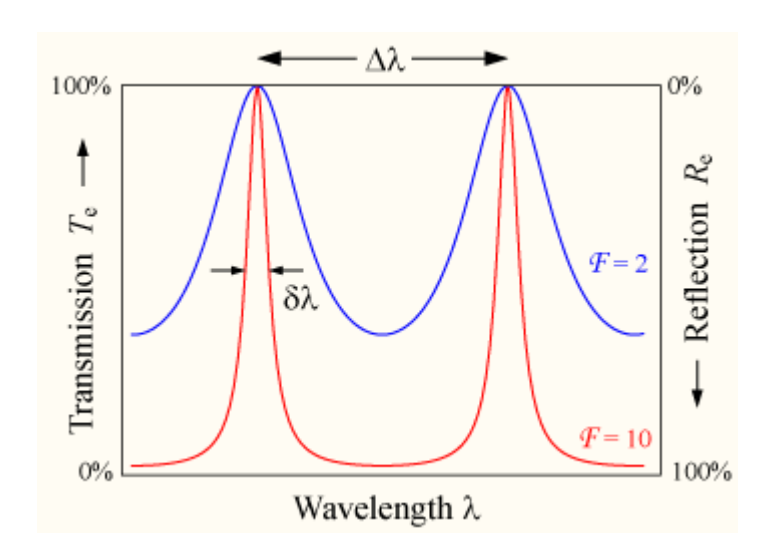


Figure 5: Transmission and Reflection peaks inside a Fabry-Perot cavity. Variation in mode linewidth due to variation in Finesse from 2 (blue) to 10 (red) [17].

The FSR ratio  $(\Delta \lambda/\lambda)$  gives us an idea of the optical cycle time with respect to the overall roundtrip time of a single beam of light to propagate around the cavity.

## 2.6.4 Quality Factor

An important aspect of the light field oscillations that needs to be taken into account is the damping factor associated with them. The Q factor (quality factor) of a resonator is a measure of the strength of the damping of its oscillations, and is also related to its relative linewidth; in simple terms it is a

measure of the mirror losses [18]. The term was originally developed for electronic circuits, e.g. LC circuits, and for microwave cavities, but later also became common in the context of optical resonators. The Q-factor is typically explained in terms of energy storage: it is  $2\pi$  times the ratio of the stored energy to the energy dissipated per oscillation cycle [19].

An equivalent definition obtained by using a simple Lorentzian approximation to the mode shape (Figure 6) is more practical: it is the ratio the resonance frequency  $f_0$  and the full width at half-maximum (FWHM) bandwidth  $\Delta f$  of the resonance peak [19]:  $Q = \frac{f_0}{\Delta f}$ 

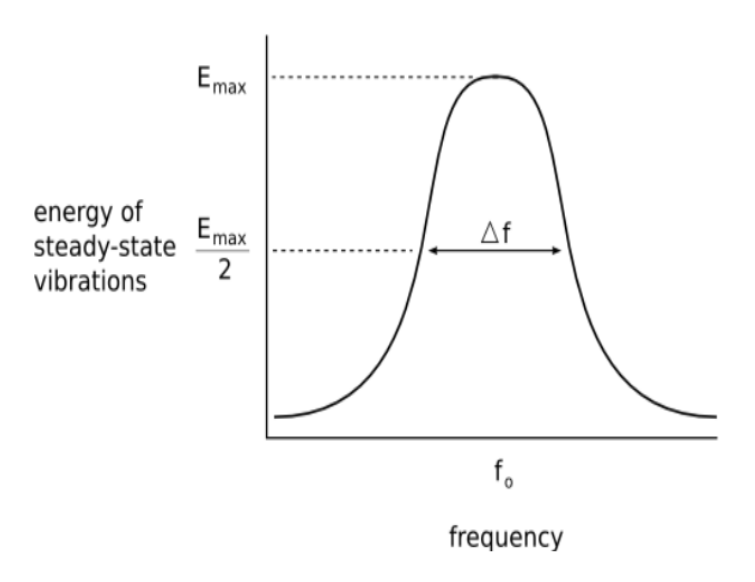


Figure 6: Lorentzian approximation to the energy distribution of the mode peak illustrating Q factor in terms of resonance frequency  $f_0$  and FWHM  $\Delta f$  [20]

The same definition works well for an optical resonator. Essentially, it compares the frequency at which a system oscillates to the rate at which it dissipates energy. A higher Q indicates a lower rate of energy dissipation relative to the oscillation frequency, so the oscillations die out more slowly. Thus, the higher the Q, the narrower and sharper the resonance peak is. In

optical resonators, it is common to define the Q-factor in terms of the wavelength and linewidth of the resonant peak as  $Q = \lambda/\Delta\lambda$ .

## **2.6.5 Finesse**

The third important parameter that we consider in terms of characterizing an optical resonator is the finesse. Similar to the quality factor, it basically measures the number of round trips until the energy stored within the peak mode decays to a factor of 1/e. The finesse is independent of the cavity length, unlike the quality factor Q [18]. The finesse is thus a separate figure of merit altogether. It is expressed as:  $F = \delta \lambda/\Delta \lambda$ .

As can be seen from Figure 5, the higher the finesse, the sharper the peaks and higher the enhancement in the ability of the optical cavity to distinguish multiple modes.

#### 2.5.6 Field Enhancement

When we pump the cavity using a certain power, the power inside it is actually enhanced. Using a generic approximation to the amount of power being circulated in the resonator relative to the incident power (assuming a steady state and that all light is being coupled into the cavity) [21]:  $P_{circ} = \frac{F}{2\pi}P_{pump}$  Thus, for a very high finesse cavity, we have a large amount of power in circulation relative to the pump power.

Furthermore, a small mode volume  $V_{mode}$  leads to higher degree of confinement of this circulating power and thus causes intensity enhancement[22]:  $I_{circ} = \frac{P_{circ}}{V_{mode}/L_{mode}}$ 

These two factors combined are instrumental in achieving low-threshold lasing in microcavities. We shall see (in chapter 5), how this factors are utilized in the design of our working device.

#### 2.7 Quantum Dot Emitters in Microcavities

Now that we have seen the emission properties and mode confinement factors associated with quantum dots and optical microcavities separately, we are in a position to look at the coupling phenomenon occurring between the gain media and the microcavity as a whole. Now we shall look at two important parameters or phenomena which govern the coupling between the spontaneous emission from the active media (quantum dot) and the optical microcavity.

## 2.7.1 Purcell Effect

The modification of a spontaneous emission from the quantum dot based on the environment surrounding the light source i.e. the optical microcavity is largely characterized by the Purcell Effect [23]. Here we look at the enhancement of spontaneous emission rates of atoms (or quantum dots) when they are matched to a resonant cavity. The maximum number of modes per unit volume occurs inside a microcavity at the mode resonant frequency. Purcell's studies show that normalizing the mode density per unit volume (of the cavity) with respect to mode density of free space, yields the Purcell Spontaneous Emission Factor [24]:  $\mathbf{F_p} = \frac{3}{4\pi^2} \left(\frac{\lambda}{n}\right)^3 \frac{Q}{V_{cavity}}$ 

With n being the refractive index of the material,  $\lambda$  the resonance peak wavelength, Q its quality factor and  $V_{cavity}$ , the effective volume of the cavity

(also expressed as  $V_{\text{eff}}$ ). An atom undergoing a transition within the mode linewidth experiences an enhancement to its spontaneous decay rate given by the Purcell factor.

## 2.7.2 Spontaneous Emission Factor

Spontaneous emission is in principle isotropic, but the modified optical density of states inside a microcavity changes this aspect. The coupling efficiency of the spontaneous emission into the resonant modes is given by  $\beta,$  the spontaneous emission factor. This can be interpreted that a fraction  $\beta$  of all the spontaneous emission stays within the cavity mode, while the rest is isotropically irradiated outside. Increasing the Purcell factor (i.e. ensuring enhanced Purcell effect) increases the coupling efficiency of the spontaneous emission with to the cavity mode  $\beta=\frac{F_P}{F_P+1}$ . Thus a high  $\beta$  is instrumental in achieving lower threshold for lasing as well as we shall see for a demonstrated device in chapter 5.

# **Chapter III**

## **Fabrication**

Rolled-up semiconductor microtubes typically are fabricated multilayered structures. Because of lattice mismatch between some of the layers there exists an inherent strain in the structures. Selective etching of a sacrificial layer results in the subsequent release and rolling of the strained layer from the substrate [25]. This fabrication process is a combination of topdown and bottom-up approaches. As their names suggest, these two approaches to fabrication and growth of material differ in terms of direction of progression with respect to the substrate. The top-down approach involves geometric definition of shapes and contours, and their eventual definition by removing material [26]. On the other hand, bottom-up assembly involves the creation of seed structures which then self-assemble into the required shape [27].

In our hybrid approach to microtube fabrication, the top-down part involves standard photolithographic steps which help us define a large number of strained mesas while giving us good control over their position and geometry. On the other hand, the bottom-up part involves the self-rolling which results in the complex three-dimensional microtube shape. In the following sections, we shall examine in detail how these microtube structures are made while incorporating quantum dot optical gain media to form lasers.

#### 3.1 Rolling in Strained Nano-Membranes

The key aspect behind formation of these tubular structures is the self-rolling that is induced, due to the inherent strain developed between the epitaxial layers, when the mesas are released from the substrate.

Let's take a look at the structure in Figure 7. When the InAs layer is pseudomorphically deposited over the AlAs layer, the larger InAs lattice constant results in a compressively strained layer. Conversely, the top GaAs layer (with a smaller lattice constant) will be tensile strained. When the AlAs sacrificial layer is selectively etched away, the strained bilayer becomes detached from the substrate. The compressively strained layer deforms to expand with a force F2, while the cap layer on top resists the expansion with force F1 (Figure 7.c). This results in a momentum (M), which drives the rolling action to form a tube in order to accommodate the relative strain within the bilayer (Figure 7.d).

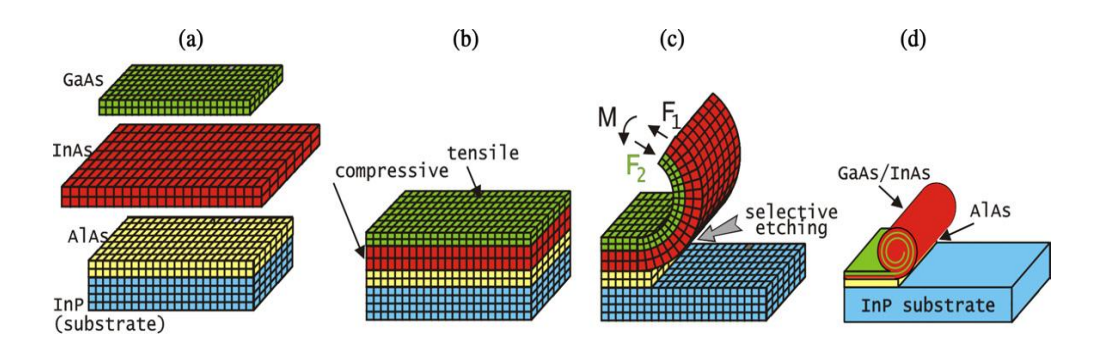


Figure 7: Illustration of the formation mechanism of strain-induced self-rolling of a semiconductor nanotube from a rectangle stripe, illustrated with an InAs/GaAs bilayer and an AlAs sacrificial layer [28]

Based on the formation mechanism, the diameter of the rolled up tube is determined by the built-in strain and the total thickness of the bilayer, and the number of rolls depends on the extent of undercutting. The inner diameter of the tube in general is estimated by a macroscopic continuum model [29]:

$$D = \frac{d(3(1+m)^2 + (1+m.n)\{(m^2 + m.n)^{-1}\})}{3\varepsilon(1+m)^2}$$
 (Eq. 2.1)

Here d represents the total bilayer thickness,  $\varepsilon$  the in-plane biaxial strain and m and n the respective thickness and Young's modulus ratios between the first and second layers While the tube diameter can be as small as a few hundred nanometers, for optical applications the diameter of the tube is typically in the range of a few micrometers with a wall thickness on the order of a few hundred nm.

The overall geometry and position of the mesa are precisely controlled by standard photolithographic processes. This includes defining a mesa region such that it will roll to produce free standing structures which will not leak light into the high refractive index substrate. A U-shaped mesa (which can be seen in Figure 8a) takes care of that [30, 31]. The rolling mechanism creates a "free-standing region" in the tube which remains propped up from the sides touching the substrate separating the central part thereby reducing optical leakage (Figure 8b). This geometry also allows for tuning the wall thickness in the free-standing part; U-shapes with longer bottom sections result in tubes with more turns and thus thicker walls. The thickness of the tube walls determine the minimum optical losses with thicker walls resulting in lower losses. As part of the mesa definition, corrugations are introduced along the mesa boundaries to create axial variations in the optical properties of the resulting microtube [31]. These corrugations allow for engineering the properties of the optical modes in the microtube, and will be discussed further

in chapter **4**. The orientation of the mesa respect to the crystalline axes is also important. Due to the crystal symmetry, the rolling will occur preferentially along the [1 0 0] crystal axis in III-V materials.

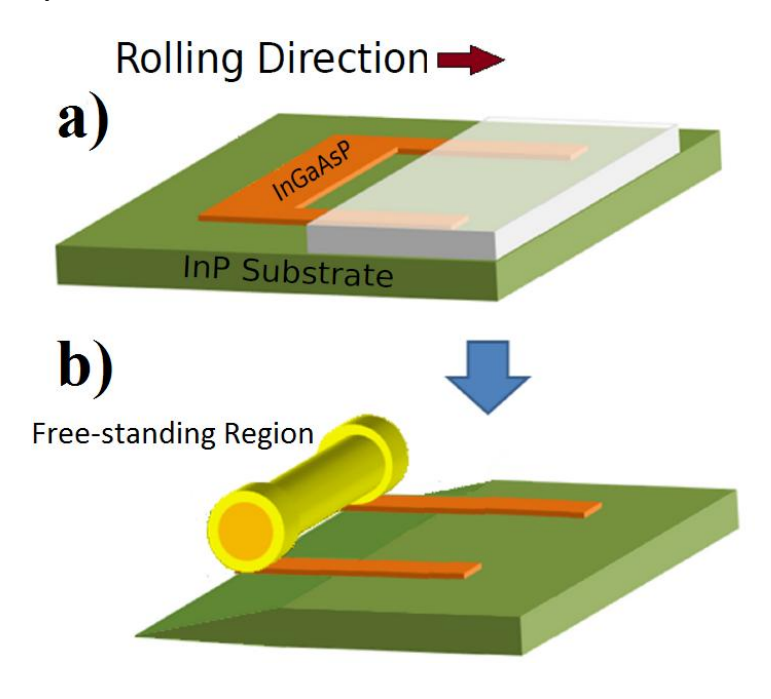


Figure 8: a) U-shaped InGaAsP mesa definition. b) Post-rolling microtube with free-standing section.

Thus, it is necessary to start from a strained nano-membrane. In semiconductors, these are usually grown by pseudomorphic epitaxy. As mentioned before, for optical purposes, III-V compound semiconductors are the material of choice due to their direct bandgap and excellent optical properties. In order to achieve emission in the technologically relevant 1.55 µm wavelength range (where standard telecommunications optical fiber has minimum loss), InP becomes the standard substrate. The epitaxial growth approach is also essential in incorporating quantum dots or quantum wells as active light emitting materials (in the form of stacks or arrays) into the tube walls.

# 3.2 Layered Microtube Heterostructure:

The first layer is made of  $In_{0.81}Ga_{0.19}As_{0.41}P_{0.59}$ , lattice matched to the InP substrate, and is 38 nm thick. Two layers of self-assembled InAs quantum dots are grown within this first layer. These are grown using the process used for more conventional quantum dot lasers [32]. A second layer of  $In_{0.68}Ga_{0.32}As_{0.41}P_{0.59}$ , with a composition chosen so there will be a built-in tensile strain, is then grown on top (Figure 9). When the InP substrate is selectively etched away, the layer will roll into a microtube. The layer thickness and composition were chosen so that the final microtube diameter is around 5  $\mu$ m (roughly calculated using Eq.2.1). The quantum dot size and composition were selected so that the wavelength of the photoluminescence emission after the rolling process peaks near 1.55  $\mu$ m

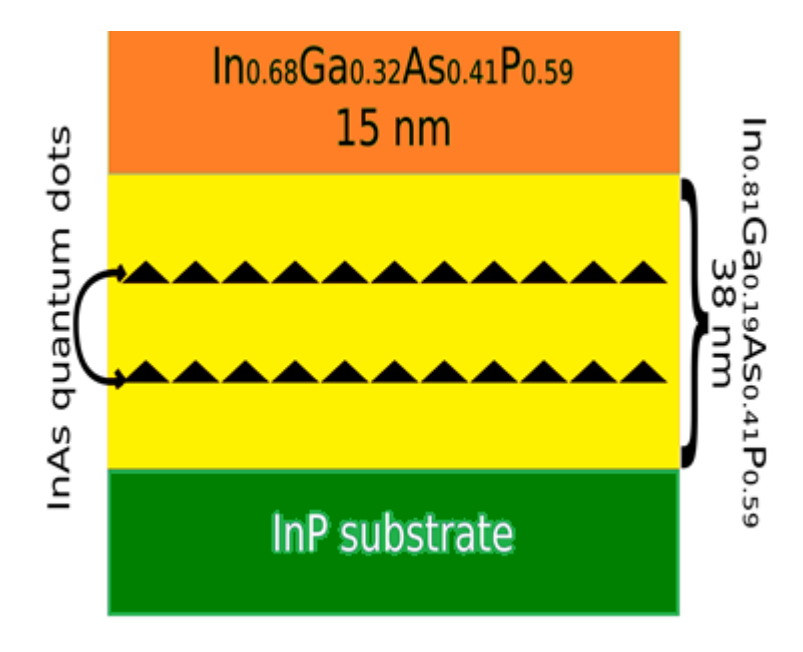


Figure 9: Schematic of InGaAsP/InP Layered Structure

This self-rolling effect induced by a single photolithographic step has been demonstrated across multiple material combinations, not only InGaAsP

multilayers. For example, it has been shown in  $In_xGa_{1-x}As/GaAs$  [33],  $Ge_xS_{1-x}As$  [34] and  $In_xGa_{1-x}As/Cr$  [35],  $SiO_x/SiO_2$  [36], etc..

# 3.3 Fabrication of InGaAsP Microtubes

The fabrication was done on the as-grown samples described in the previous section. Standard optical lithography (using Shipley S1813 photoresist) and a non-selective wet etch (HCl:HNO<sub>3</sub>:H<sub>2</sub>O 1:2:1) were first performed to define the mesa layer (see Appendix I for a detailed list of the process steps). The mesa orientation is key here to ensure rolling in the [1 0 0] direction.

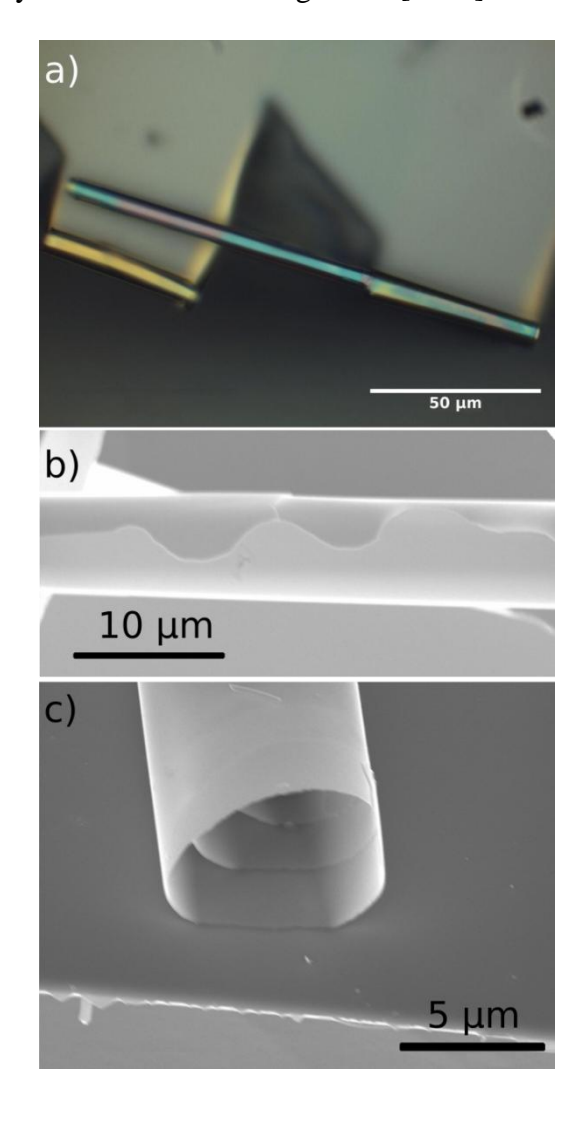


Figure 10: a) Free-standing InGaAsP rolled-up microtube. b) SEM image illustrating periodic corrugations along the sides of the tube. c) SEM image illustrating the number of turns in a particular device-3.

Following the mesa definition, selective etching of the InP substrate is done using an HCl:H<sub>2</sub>O 2:1 solution while the extended sections or "legs" of the mesa are protected using photoresist (again, see Appendix I for detailed process steps). The sacrificial etch removes part of the substrate without significantly affecting the mesas and results in the rolled-up microtubes. Special care however needs to be taken to dry the tube structures, following the sacrificial etching since direct rinsing with water presents a likelihood of breaking the devices. It should be noted that in this fabrication process no special sacrificial layer is needed, so the gap between the free-standing part of the microtube and the substrate is not limited by the thickness of a sacrificial layer. This means that no extra processing is needed to minimize optical leakage. Varying the etching time results in changing the extent of undercutting producing 1,2 and even 3 turn tubes (as illustrated in Figure 10c).

# **Chapter IV**

# **Photoluminescence Studies**

In order to characterize the optical properties of the microtubes described in the previous chapter, we have performed photoluminescence (PL) measurements. In this chapter we will describe the experimental setup that was used and the relevant results we obtained.

#### 4.1 Photoluminescence

By shining an incident laser light (excitation source), the electrons of the gain media (quantum dots) are excited to a higher state due to absorption. Eventual decay of these electrons to their respective ground states is in the form of fluorescence or radiative decay, producing photons. The emission spectrum of the PL is strongest at energies corresponding to the discrete energy levels in the quantum dots. The spectral properties will be modified by the microtube cavity: when coupled to the microcavity resonant modes, the emission will display sharp peaks.

# **4.2 Experimental Setup**

In this section, we describe the experimental setup used to conduct PL studies on our InGaAsP microtube devices.

Figure 11 represents a schematic of the PL setup designed and used for the study of our InGaAsP microtubes. We used a continuous wave red-laser diode (635 nm emission wavelength) as the excitation source. The beam from this laser was chopped using a mechanical chopper and sent through a dichroic beam splitter to a microscope objective (100×, 0.70 NA). This objective

focused the pump light on the microtube sample, which was held on a mechanical stage (and optionally inside a cryostat for low temperature studies). The PL from the microtubes was collected with the same objective and directed to a grating spectrometer by the dichroic beam-splitter. A long pass filter was used to block any remaining pump light. The spectrometer dispersed the incoming PL and, using a slit, let only a narrow spectral bandwidth to fall onto a liquid-nitrogen-cooled InGaAs photo-detector. The signal from the detector was amplified using a lock-in amplifier locked at the frequency of the mechanical chopper and measured using a computer. By scanning the grating in the spectrometer, full spectra of the PL could be measured. See Appendix II for details on the alignment and measurement procedure.

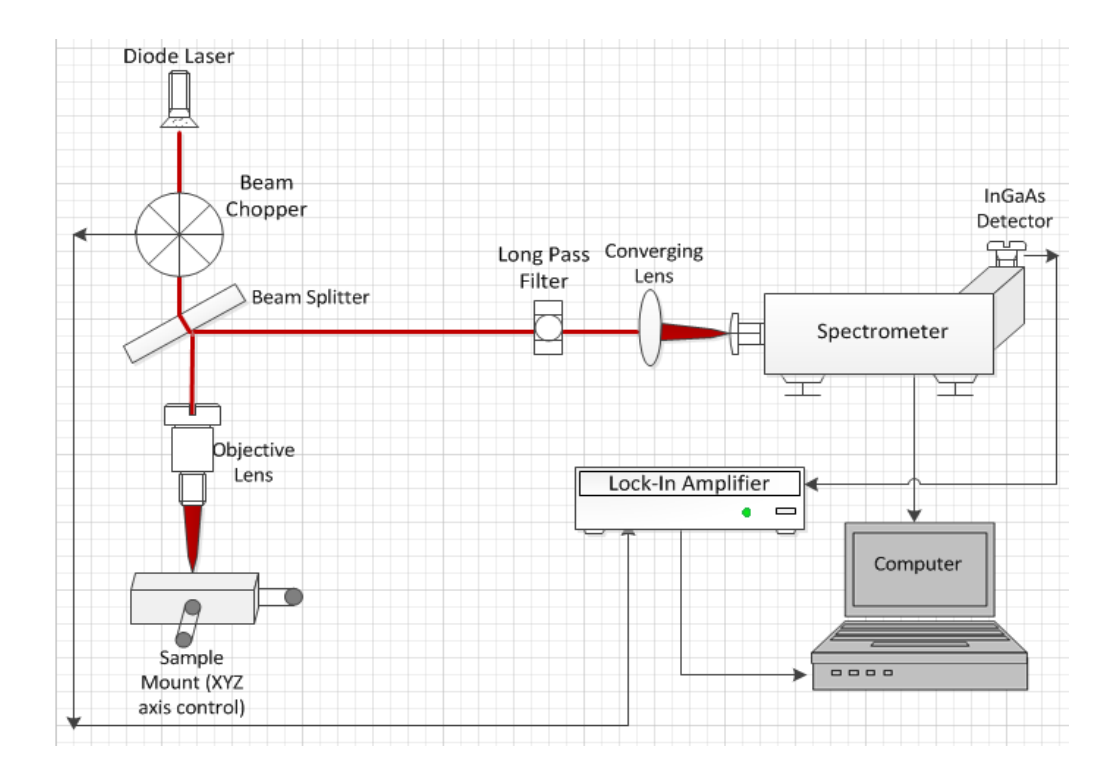


Figure 11: Schematic of PL setup used and its components

# 4.3 PL Spectroscopy of a single InGaAsP microtube

The PL spectra observed from the sample before (as-grown) and after rolling (with rolled up microtubes), yielded some interesting results. For comparison purposes, the spectra observed around the same wavelength range is illustrated in Figure 12 (as-grown) and Figure 13 (rolled-up microtube) respectively.

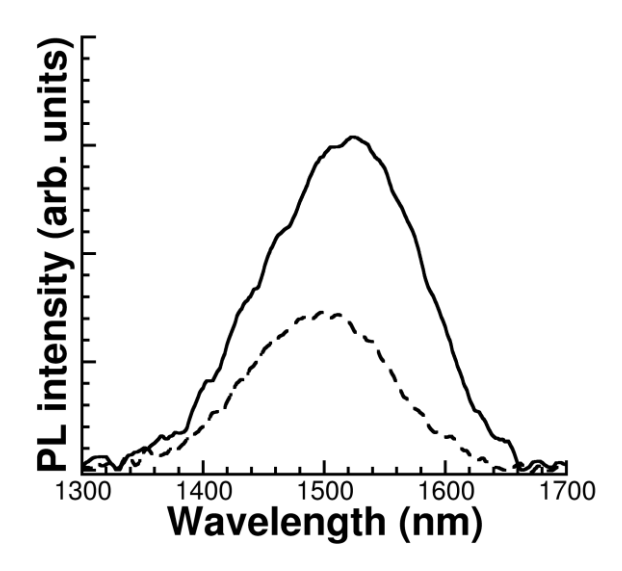


Figure 12: PL spectra for the as-grown sample (dashed line) and a rolled, non-free-standing microtube (solid line) measured at room temperature.

The emission at room temperature ( $\sim 300~\text{K}$ ) from the bare sample (as-grown) yields a broad spectral emission centered at  $\sim 1.5~\mu m$  (the dashed trace in Figure 12). This is in accordance with the expected InGaAsP/InAs quantum dot layer emission as discussed in chapter 2. The quantum dot ensemble shows a large inhomogeneous broadening, covering a range of wavelengths from 1.3-1.7  $\mu m$ , because of the large variation in the sizes of individual dots. Emission from a non-free-standing section of a rolled-up microtube, under similar conditions, yields an interesting observation. There is a distinct shift in the central wavelength of the emission to higher wavelengths (red shift). This is

attributed to the quantum dot levels shifting to lower energies due to the release of strain brought about by the rolling mechanism [37]. The microtube spectrum is red-shifted approximately 20 nm from the flat piece spectrum, but it is otherwise similar. The emission is also stronger, since due to the rolling there are more quantum dots in the excitation area.

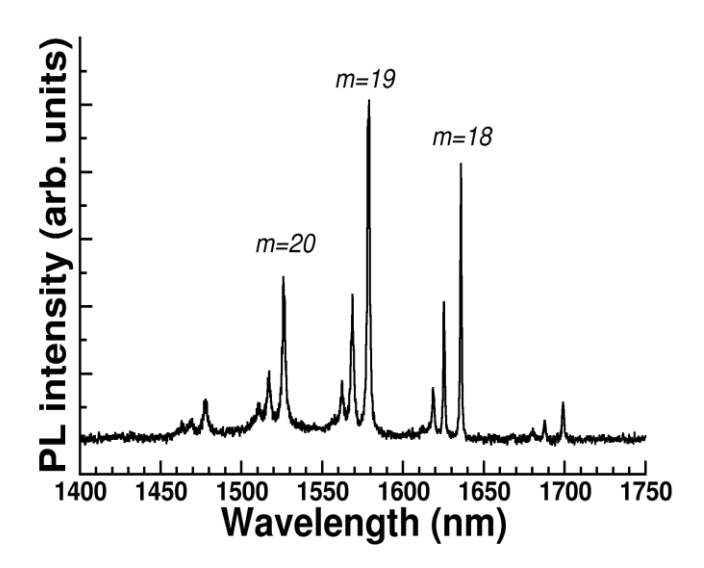


Figure 13: Rolled-up Microtube (RUMT) PL emission from free standing region of two turn sample. The mode azimuthal number is denoted by (m).

Emission from the free-standing part of the microtube, shown in Figure 13, reveals the presence of sharp peaks now instead of the broad as-grown emission spectra. These sharp peaks appear in groups, where each group corresponds to a different azimuthal mode number (m) and each peak in a group corresponds to a different axial mode caused by the corrugations in the outer edge.

The mode numbers have been identified by applying a model where the microtube is unrolled and considered as a planar waveguide with periodic boundary conditions which will be discussed in the next section[38, 39].

# 4.4 Modelling Microtubes as Optical Cavities

In order to achieve a microtube based quantum dot laser, it is necessary to understand the effect of design parameters, such as the tube diameter and wall thickness, have on the optical properties. To first order, a microtube can be approximated as a two-dimensional ring resonator [40]. However, the spiral geometry of microtubes can introduce some subtle differences with this simple approximation (Figure 14). In particular, the addition of axial confinement via the surface corrugations introduced during fabrication requires a more sophisticated model.

# Outside notch

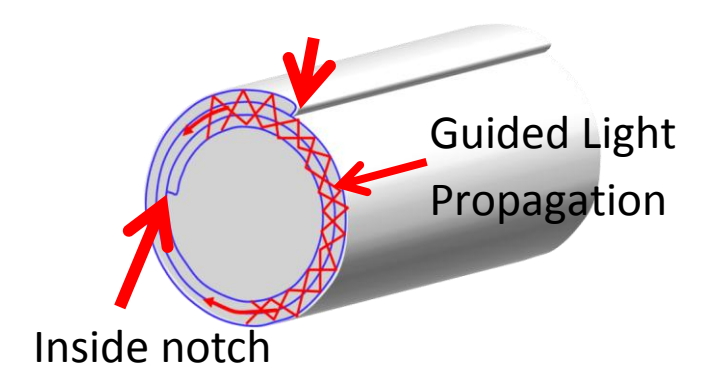


Figure 14: Microtube bottle resonator illustrating light propagation due to effective wave guiding (red).

One such model, which still remains computationally efficient, involves considering the microtube wall as an effective planar slab waveguide. Post rolling, the tube consists of two different wall thicknesses and two points or notches at which the wall thickness changes (see Figure 15). The effective planar waveguide is then composed of two slabs with different thicknesses

(and a step that has a z-dependent shape). This composite waveguide can be analyzed using a straightforward procedure.

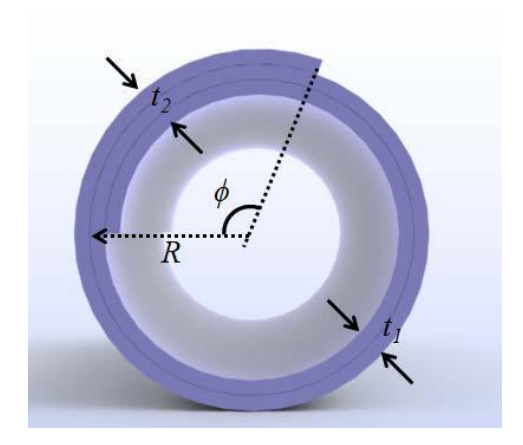


Figure 15: Cross-section of a microtube showing the two sections with different wall thicknesses and the inner and outer notches [41].

At a given z position, we can think of the equivalent waveguide as composed of two parts with lengths  $L_{thick}(z)$  and  $L_{thin}(z)$  so that  $L_{thick}+L_{thin}=2\pi R$  (R is the diameter of the tube) and effective refractive indices  $n_{thick}$  and  $n_{thin}$  respectively which are computed using the well-known solutions for planar slab waveguides. Then, we can take the full waveguide as having an average effective index  $n_{circ}(z) = L_{thick}(z)n_{thick} + L_{thin}(z)n_{thin}$ . From this, we obtain a two-dimensional planar waveguide with a single refractive index which varies in the z direction. Since the polarization of the emission in thin walled tubes is predominantly along the tube wall (the z axis), we can analyze the modes by applying the scalar Helmholtz equation to the waveguide:

$$-\frac{1}{n_{circ}(z)^2} \left( \frac{d^2 E(l,z)}{dz^2} + \frac{d^2 E(l,z)}{dl^2} \right) = k^2 E(l,z) \quad (Eq. 4.1)$$

Where E(l,z) is the electric field and  $k=2\pi/\lambda$  is the vacuum wavevector. Assuming separation of variables (which is a good approximation as long as the axial variation is weak), we can substitute the ansatz E(l,z) =  $\varphi(z)\exp(i\beta l)$  and obtain (after application of the boundary conditions) the azimuthal resonance condition.

$$\beta R = m, (Eq. 4.2)$$

The azimuthal resonance condition, and

$$-\frac{\partial^2 \phi}{\partial z^2}(z) - n_{circ}(z)^2 k^2 \phi(z) = -\beta^2 \phi(z), \quad \text{(Eq. 4.3)}$$

which is formally similar to the Schrödinger equation and thus usually called the "photonic quasi-Schrödinger equation" [39]. Each one of the solutions to Equation 4 corresponds to a different axial mode, which is labeled by the axial mode number p. Combining Equations 4.2 and 4.3; we can compute the complete resonance spectrum of a microtube with an arbitrary corrugation shape (as shown in Figure 16).

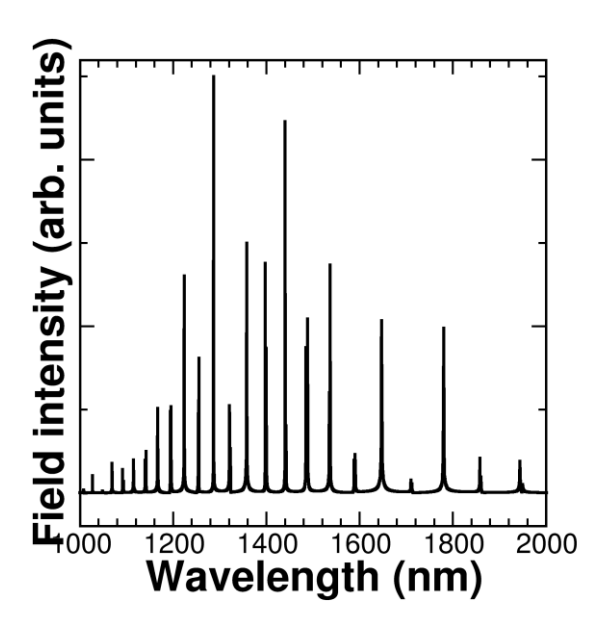


Figure 16: Complete resonance spectrum of InP microtube computed from the quasi-Schrödinger wave equation.

From this model, it can be seen that controlling the shape of lobes on the rolling edge will change the spectrum of the axial modes, as has been experimentally demonstrated [31, 39]. In particular, we can use physical intuition to realize that high curvature, deep, corrugations will result in more separated axial modes, while low curvature, shallow, corrugations will show less separation between consecutive axial modes. Regarding losses, in this structure, the two major loss mechanisms are the bending loss from the curvature of the microtube wall and the scattering losses that occur at the discontinuity in the two notches.

#### 4.5 Discussion

Armed with a better understanding of the resonant modes, we can analyze the spectra from free-standing microtubes such as the ones in Figure 17. For both spectra, the spacing between groups (~ 6500 GHz or 27 meV) is consistent with a tube diameter near 5 µm. The bottom spectrum in Figure 15 is from a tube formed by one turn of the membrane. The small thickness of the wall results in large bending losses, and broadening of the modes. The large spacing between the axial modes (~ 9.5 meV) means that the corrugations in this tube have a high curvature, providing strong confinement and smaller mode volumes resulting in larger spectral spacing [30].

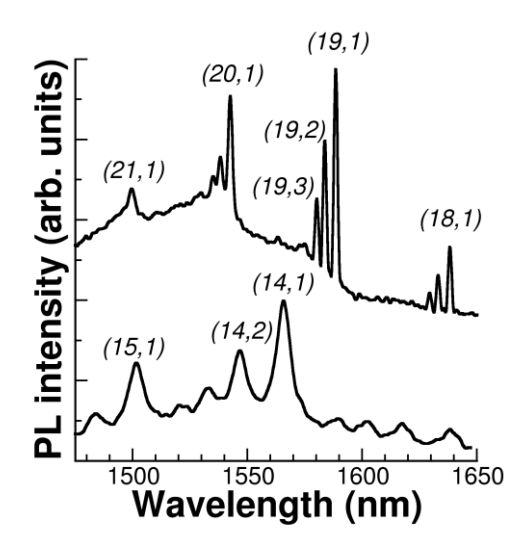


Figure 17: Rolled-up Microtube (RUMT) PL emission from free standing region of two turn (top) and one turn (below) samples. The mode azimuthal and axial mode numbers are denoted in the order (m,p).

The spectrum of a two-turn tube (Figure 17), shows much narrower modes than the one turn spectrum we have just discussed, indicating that tubes with thicker walls have smaller losses. In this tube, the spacing between the axial modes is small, closer to 2.3 meV. This indicates the corrugations in this tube have a low-curvature, since they will provide weaker confinement and larger modal volume and thus yield smaller spectral spacing. The emerging trend is that thicker walls correspond to lower losses, in particular considering the very high cold-cavity Q-factor of 1.5×10<sup>5</sup> previously measured in a five-turn InGaAs/GaAs tube (with a wall thicker than 250 nm) [42].

### 4.6 Optical Field Distribution

It is possible to do a more sophisticated modeling of the fields in the resonant modes in the microtube. Depending on the dominant optical field components inside the tube wall, the modes can be classified as transverse electric (TE) and transverse magnetic (TM). (Figure 18)

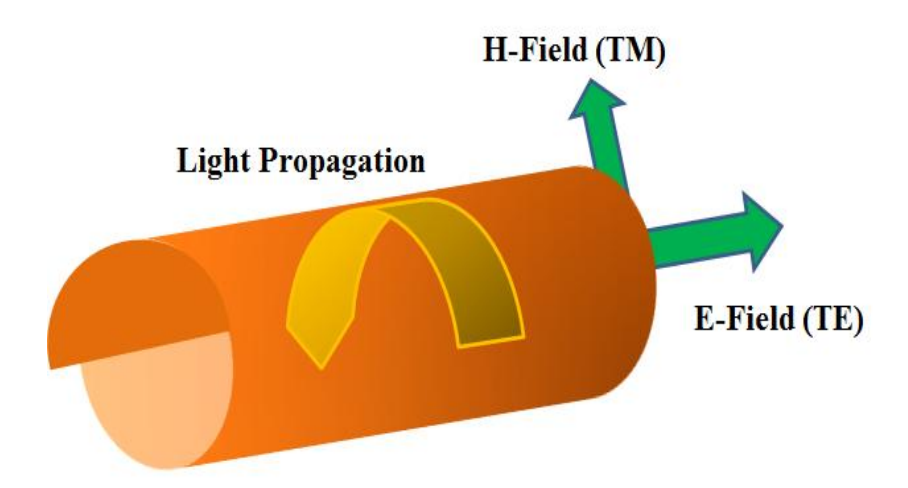


Figure 18: TE polarized distribution with electric field parallel to tube axis and TM polarization normal to the tube wall.

The TE modes dominate in terms of emission while the TM modes are less pronounced due to losses brought about by weaker confinement and higher susceptibility to losses along the tube walls. As demonstrated by Strelow *et al.*[39], Maxwell's equations are used to determine the scalar wave equations of the z-component of the electric field in terms of the refractive index of the medium n and the vacuum wavevector k.

$$-\frac{1}{n^2(r,\phi,z)} \nabla^2 E_z(r,\phi,z) = k^2 E_z(r,\phi,z) \qquad \ (\text{Eq. 4.4})$$

Cylindrical coordinates  $(r, \phi, z)$  are used to describe the light propagation in both the plane of circumference  $(r-\phi \text{ plane})$  as  $k_{circ}$  and in the axial plane (due to continuous reflections of light from the end facets) as  $k_z$ , such that.

$$k^2 = k_{circ}^2 + k_z^2.$$

An adiabatic (Born-Oppenheimer) approximation [43] to the electric field component in the z-plane is then made to describe propagation in the two planes  $E_z(r,\phi,z)=\Phi(r,\phi,z)\Psi(z)$ , with  $\Phi(z)$  and  $\Psi(r,\phi,z)$  denoting the

solution to the circulating propagation (along the circumference, for a fixed z) and the axial propagation respectively.

This introduces the concept of treating electromagnetic waves in terms of confined optical particles and the condition for circulating propagation at any fixed point z along the length of the tube, given by:

$$-\frac{1}{n^{2}(r,\phi,z)}\nabla_{r,\phi}^{2}\Phi(r,\phi,z) = k_{circ}^{2}(z)\Phi(r,\phi,z)$$
 (Eq 4.5)

Eigen values of this represent the azimuthal mode numbers denoted by m. combining the solutions to Eq. 4.5 and the above description of the wave vector k, the photonic quasi-Schrödinger wave equation is developed (again) to characterize the electromagnetic field distribution in the r- $\varphi$  plane for fixed values of z.

$$-\frac{1}{n^2} \frac{\partial^2}{\partial z^2} \Psi(z) + k_{circ}^2(z) \Psi(z) = k^2 \Psi(z)$$
 (Eq.4.6)

This equation describes the axial mode distribution with the solutions characterized by wavevector component  $k_z$ , with axial mode number p. The circular propagating parameter  $k_{\rm circ}(z)$  defined by the solutions to Eq 4.5, acts as a quasi-potential  $V_{\rm eff}(z)$  for the axial propagation. The planar waveguide approximation previously mentioned considers the microtube as two coupled planar waveguides of thicknesses  $t_1$  and  $t_2$  and lengths  $L_1$  and  $L_2$  such that  $L_1+L_2=2\pi R$  (circumference of the tube) as shown in Figure 15. Periodic boundary conditions are then applied to the ring-shaped cross section (with discontinuous outer and inner notches) and ensure phase matching of light after one round trip.

Strelow [39] and others report that the circulating propagation vector  $k_{circ}$  depends linearly upon the quantity  $p(z) = \frac{L_1(z)}{L_1 + L_2}$  with a deviation of approx.

0.1%. Using this relation together with design or experimental data, it is possible to write explicitly the effective potential  $V_{\rm eff}(z)$  and solve (usually numerically) Eq. 4.6. The validity of the adiabatic approximation [43] holds under the condition that  $\Delta k_z^2 \ll |(k_{circ}^m)^2 - (k_{circ}^{m+1})^2|$  is satisfied with  $\Delta k_z^2 = |(k_z^h)^2 - (k_z^{h+1})^2|$ . Experimental data from typical microtubes shows that this is indeed the case.

# 4.7 Finite Difference Time Domain (FDTD) Simulation Results

We also performed two dimensional (2D) finite-difference time-domain (FDTD) simulations of TE modes in a rolled up structure, with results shown in Figure 19. The calculated field patterns confirm the whispering gallery behaviour of the modes in the microcavity. The simulations were performed for two different tubes: one with an 84 nm thick wall (Figure 19a) and another with a 126 nm thick wall (Figure 19b).

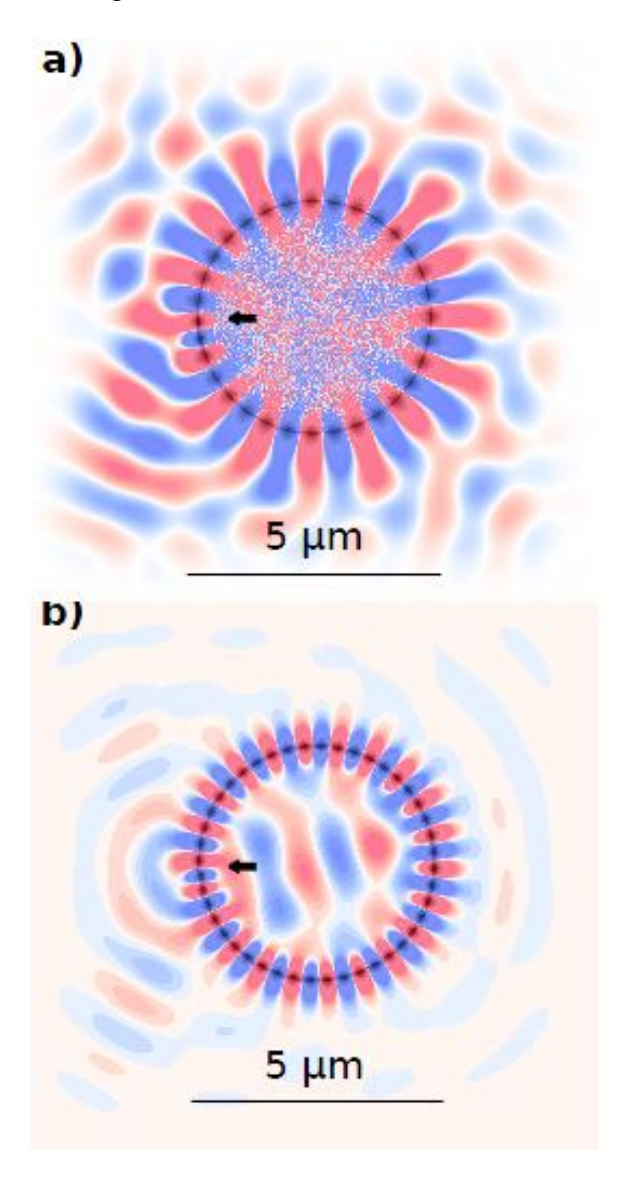


Figure 19: a) Electric field distribution of a 2-turn 84 nm thick tube wall, with azimuthal wave number m=16 at resonant wavelength 1463 nm. The inner notch characterizes the directional nature of the emission. b) Electric field distribution for a 3-turn 126 nm thick tube wall, with m=22 at resonant wavelength 1440 nm showing better directional emission due to presence of inner notch. The notch is indicated by the arrow (in both cases).

We see clear confinement of the electric field in both cases depicting azimuthal lobe characteristic of a whispering gallery mode. The thinner-walled (Figure 19a) displays higher leakage of field, outside the tube walls and thus more losses. The presence of the inner notch gives a slight directionality to the emission pattern. The thicker-walled tube (Figure 19b) shows much reduced exterior fields, resulting in fewer losses with the inner notch dominating the radiation, giving highly directional emission. The simulation analysis confirms what we saw in the optical characterization data: tubes with thicker walls show less loss.

# Chapter V

# Rolled-Up InGaAsP Microtube Laser

### **5.1 Introduction**

In the previous chapters we have discussed the fabrication and optical characterization of InGaAsP rolled-up microtubes with InAs quantum dots embedded in their walls. We have seen evidence of good optical confinement and strong emission from the quantum dots. That means that the microtubes are good optical cavities, while the quantum dots are optically active and could act as a gain medium. Since we now have the two basic components of a laser (a resonator and a gain medium), it follows logically that an InGaAsP microtube laser should be feasible.

# 5.2 Power dependence of the emission at low temperature (82 K)

Since non-radiative recombination in quantum dots is suppressed at lower temperatures and thus the PL intensity (and correspondingly, the gain) is increased, it makes sense to look for lasing at low temperatures. In order to do this, the microtube was mounted on a cryostat chamber for performing PL spectroscopy and extensive power dependent measurements were carried out using the micro-PL  $(\mu$ -PL) procedure described in Appendix II.

The chamber was cooled down to 82K, inducing a significant blue shift in the PL spectra (~100 nm). This is primarily due to the bandgap change of the active emission material i.e. InAs quantum dots, following Varshni's empirical formula for temperature dependence [44]. The spectra observed was also considerably brighter (higher output signal recorded for constant input

excitation powers), confirming the reduced non-radiative recombination losses. A look at the emission spectra illustrating the modes at two different pump powers (Figure 20a), of (low) 180 nW and (high) 5.8  $\mu$ W, indicates an increase in the peak area of the central peak at 1470 nm (mode numbers m=22, p=1) with increasing pump power. This peak, when compared to the adjoining peak at 1447 nm (mode numbers m=22, p=4) exhibited a jump in terms of the peak area vs. the pump power absorbed (Figure 21a and b). Moreover, when comparing the emission of the flat sample with the rolled up tube emission (Figure 20a), we observed low background emission and clear mode structures indicating efficient coupling of the quantum dot PL to the optical modes.

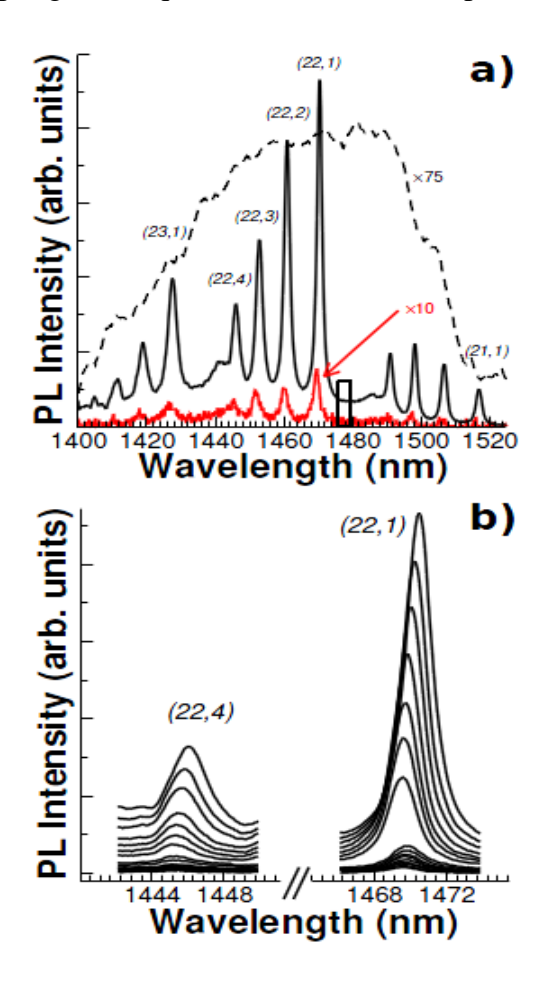


Figure 20: a) Photoluminescence spectra of an InGaAsP microtube at 5.6  $\mu$ W (black) and 180 nW (red) under low temperature (82 K) conditions. The dashed curve represents the spectrum of an as-grown sample under same conditions and the box illustrates a point 8 nm away from the mode to obtain background emission characteristics. b) Evolutions of spectra of modes (22,1) and (22,4) with increasing absorbed pump power.

Using peak fitting software [45], the peak features were extracted from each spectrum and fitted using Lorentzian functions to obtain a quantitative description. From the fits, the dependence of the peak area and the full-width-at-half-maximum (FWHM) on the pump power was obtained. The results are shown in Figure 21, for two different modes.

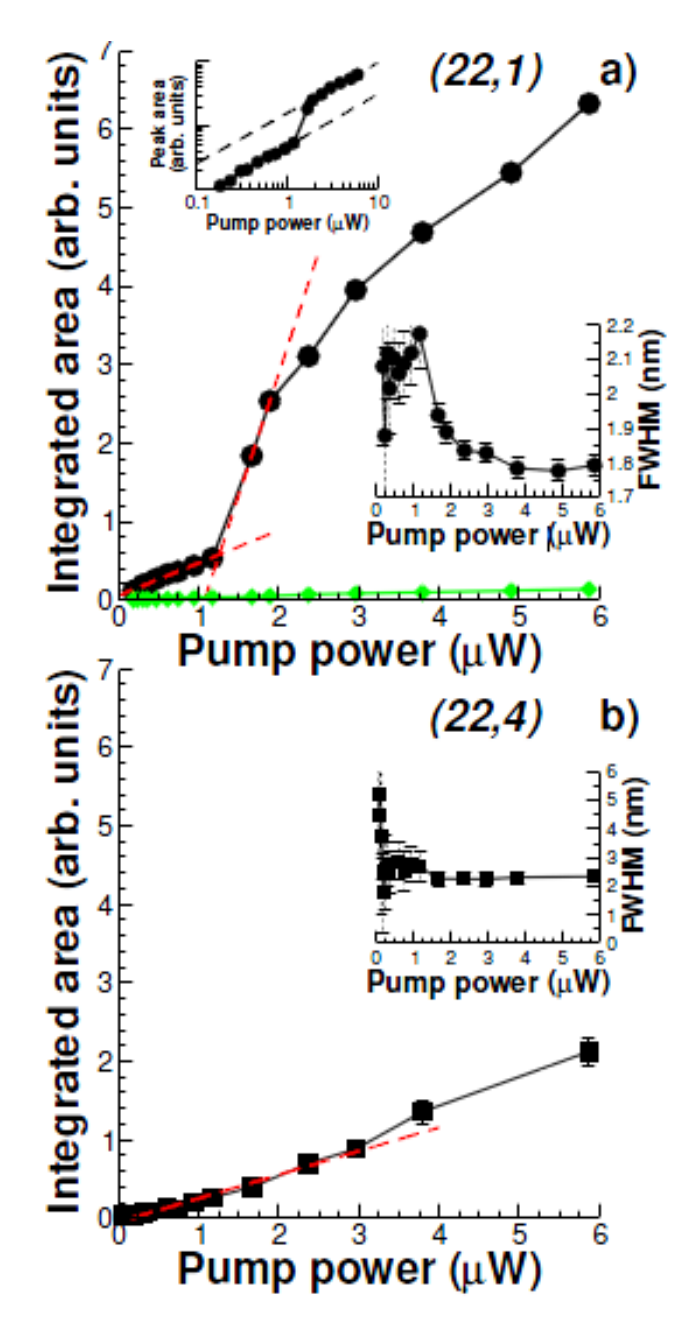


Figure 21: a) Peak integrated area curve for mode (22,1) and the emission from the background (green) vs. Pump Power. Lower Inset: FWHM of the (22,1) mode illustrating abrupt decrease after threshold to confirm lasing. Upper Inset: Peak area vs Pump power intensity plot in Log scale clearly showing threshold. b) a) Peak integrated area curve for mode (22,4) indicating no significant decrease in peak linewidth at high powers.

Figure **21a** illustrates the lasing phenomenon clearly in mode (22,1) with the occurrence of a kink in the integrated area vs. pump power plot, setting the threshold at 1.26  $\mu$ W for mode (22,1). At the higher pump powers there is a roll off of the peak area which can be attributed to heating of the microtube.

A significant narrowing of the linewidth of the mode is also seen in Figure 21a (from 2.2 nm to 1.8 nm) starting at the threshold pump power, denoting the increasing temporal coherence of the emitted light. This further suggests the lasing phenomenon for this mode.

The same data for peak (22,4), in Figure **21b**, shows no evidence of lasing, with a smooth peak area versus pump power curve and no significant reduction in the peak linewidth at higher powers.

Background emission from a distance of 8 nm from the central peak (22,1) (see Figure 20a) was obtained by subtracting the fitted modes from the measured photoluminescence for each pump power and plotted (green diamonds in Figure 21a). The background emission increases linearly with respect to pump power, however the slope of the curve is scaled down by a factor of 100 when compared to the slope of the emission curve for mode (22,1). The phenomenon of stimulated emission is demonstrated here, as the increase in the rate of photons produced by increasing pump power is much higher in the mode integrated area emission than the background.

Using the value of the excitation threshold power  $P_{th}$ =1.26  $\mu$ W a rate equation model [46] is used to calculate the fraction of spontaneous emission coupled to the optical mode  $\beta$ . From the model, we know that:

$$\frac{P_{th}}{\hbar\omega_p} = \frac{\omega_c}{(Q\beta)(1 + \tau_{sp}/\tau_{nr})}$$

Where,  $P_{th}$  is the threshold absorbed power of the laser,  $\omega_p$  the oscillation frequency of the pump laser ( $\lambda_p = 635$  nm),  $\omega_c$  the oscillation frequency of the central peak ( $\lambda_c = 1470$  nm).

Assuming the non-radiative recombination rate to be negligible (lower bound on  $\beta$ ), we used a quality factor value of Q=1400, from the linewidth of the mode, right before threshold and considering a doublet [31]. Using these values, and assuming 75% absorption of the excitation pump power, we calculate a  $\beta$  value of 0.30. This is a lower bound, since the actual absorbed power in the dots can be lower than the measured incident threshold power. The Purcell factor (Chapter 1), is also calculated using:

$$F_{P} = \frac{3}{(4\pi^{2})} \left(\frac{\lambda_{c}}{n_{eff}}\right)^{3} \frac{Q}{V_{eff}}$$

The values for  $n_{eff}$  and  $V_{eff}$  are estimated using the planar waveguide model to be  $n_{eff} \sim 2.09$  and  $V_{eff} \sim 8.5~\mu m^3$ . Using these values, we calculate an enhancement factor  $F_p \sim 4.8$ 

# 5.5 Conclusion

We have demonstrated laser emission from rolled-up InGaAsP microtubes with InAs quantum dot under optical pumping at cryogenic temperatures. This demonstration shows their potential as light sources. Considering other attributes, such as the capability for integration [42], InGaAsP microtubes are candidates as laser sources for chip-level optical and integrated optical communications [47, 48]. Power-dependent characterization reveals a lasing threshold power of  $\sim$ 1.26  $\mu$ W from microtubes with a diameter of  $\sim$ 5  $\mu$ m and a

wall thickness of ~100 nm, and the observed optical modes are analyzed using an equivalent planar waveguide model. The FDTD simulation analysis confirms the whispering gallery character of the modes and our initial observations from experimental data: tubes with thicker walls show less loss. Thus a thicker walled tube would be more appropriate for lasers, with lower losses and lesser sensitivity to surface imperfections. Future work will focus on improving the fabrication and lasing characteristics to obtain room temperature lasing and on fabricating and characterizing electrically injected devices.

#### APPENDIX I

#### **Fabrication of InGaAsP Microtube**

# **Sample Structure Description:**

In this case, the system consists of strained 24 nm  $In_{0.81}Ga_{0.19}As_{0.41}P_{0.59}$  and 12 nm  $In_{0.68}Ga_{0.32}As_{0.41}P_{0.59}$ , containing two layers of self-assembled InAs quantum dots.

# **Preparation**

The actual preparation process starts with defining the U-shaped strained mesa by etching into the strained InGaAsP layer:

- 1. Prepare a solution of HCl:HNO<sub>3</sub>=30:60(1) and let it react for 30 minutes until its color turns bright red
- 2. Dilute solution (1) by adding water to it to water to form:  $HC1:HNO_3:H_2O=30:60:300(2)$ .
- 3. Cut a piece of the as-grown wafer and cleaned it with Acetone (5 min), IPA(2 min) and DI water. Dry it with clean nitrogen gas.

# Lithography step 1: U-Shaped Mesa

The alignment (45 degrees with the sample cleaved edge) is crucial for this step.

- 1. Bake the sample at 115  $^{0}\text{C}$  for 5-10 min. Spin coated a 1.4  $\mu m$  layer of Shipley S1813 positive photoresist.
- 2. Do a post-coating soft-bake at  $115\,^{0}$ C for 1 min.
- 3. Use the "Optimized U-shape" mask to expose the sample (taking care that the mesas form a 45 degree angle with the sample cleaved edge) and expose using hard contact and a 70 mJ/cm<sup>2</sup> dose.

- 4. Develop the sample under MF-319 for 1minute, washed with DI water and blow dry with clean nitrogen gas.
- 5. Look at the result of the photolithography under a yellow-light microscope and if it is not satisfactory, clean the sample and do it again.

# **First Etching**

- 1. Use the dilute solution (2) to etch sample (right into the substrate) for about 1 min, 20 seconds.
- 2. Following this wash the sample with DI water and blow it dry. Remove the photoresist using acetone (3 min), IPA(1 min) and DI water.
- 3. Blow the sample dry again and measure with the profile-o-meter to make sure that the etch depth reached substrate level.

# Lithography 2: Protecting the U-shaped Mesa

The side pieces of the U-shaped mesa are protected using a layer of photoresist.

- 1. Bake the sample at 115  $^{0}$ C for 5-10 min. Subsequently, deposit a 1.4  $\mu$ m layer of S1813 using spin coating.
- 2. Soft bake the sample at 115 °C for 1 min.
- 3. Use the rectangular mesa cover mask and expose the sample with hard contact and a dose of 70 mJ/cm<sup>2</sup>.
- 4. Develop the sample in MF-319 for 1 min, wash it with DI water and blow dry it.
- 5.Inspect the sample under yellow-light microscope to verify the results. If there is a problem, start again with a fresh piece of sample.

# **Sacrificial Etching**

- 1. Prepared a HCl:H<sub>2</sub>O=1:1(3) solution.
- 2. Etch the sample in solution (3) for about 15 min. Be careful, as the sample is fragile and the etch is quite violent.
- 3. Prepare a beaker with acetone and another one with methanol.
- 4. Gently removing the sample from solution (3), dip it into acetone and methanol.
- 5. Finally, carefully immerse the sample in methanol, leaving it there for about 2 min while stirring it very gently and taking care *not* to move it around too much.
- 6. Take the sample out carefully, and leave it to dry.

# APPENDIX II

# **PL Setup Configuration**

The principal components of the PL setup are shown in Figure 11. This is the procedure to use for alignment and measurement.

# **Initial Set Up**

- Mount the laser steering mirror at the same height of the laser, at 45 degrees so the excitation laser beam is directed towards the sample stage. Try to make the laser spot hit the mirror near its center.
- 2. Install the chopper after the laser. Make sure it is off and position it so it lets the laser beam go through.
- 3. Using a reflective sample (a clean silicon wafer or a metal-coated glass slide will work) in the sample stage, make sure that the laser beam is perpendicular to the stage. This will happen when the reflected beam from the sample overlaps with the beam at the output of the diode.
- 4. Mount the beam-splitter below the laser steering mirror at an approximate angle of 45 degrees (with respect to the stage mount). Check the mirror height to ensure that the reflected beam from the sample enters into the spectrometer in a straight line after being reflected off the beam-splitter.
- 5. Mount the objective below the beam-splitter, making sure there is enough space to turn the objective mount screws. Make sure the objective lens itself is perpendicular to the incident laser beam by putting a reflective sample on top of it and controlling its tilt until the reflected spot overlaps with the laser diode output.

6. Fine-tune the beam splitter angle such that the light reflected of the sample reaches the slits in a straight-line and is centered on the entrance slit.

# **Alignment:**

The alignment section details the actual steps taken to ensure maximum accuracy of data collection. The following steps describe the illumination process of the tubes, the optimization of the reflected beam and finally the data collection aspects in details.

- 1. Mount the sample (consisting of rolled-up tubes) by placing it on a glass slide/flat holder atop the sample mount. Check the image produced by shining the laser beam on a tube and makes sure the tube (image) is perpendicular to the entrance slit (along its length, Figure 10a). In order to achieve this ensure that the mesa-rows on the sample (viewable on the sample minutely) are located parallel to the spectrometer slit.
- 2. Use a paperboard (white) screen in front of the beam splitter to roughly estimate the position of the mesa (and the tube) under consideration. Typically with the 100x objective, an image can be seen keeping the screen ~30 cms away.
- 3. The parabolic surface corrugation is expected to be located near the center of the free standing part of a tube (Chapter 3, Figure 10b). Select a spot on the central free-standing region and focus the laser beam on it. Use the XYZ mount-screws to move the sample so that the

- beam moves along the tube (lengthwise) and across the tube width (perpendicular) to select subsequent such spots.
- 4. Set the lock-in amplifier to the same frequency as the chopper (usually the lock-in amplifier reference is connected to the chopper driver). Using the spectrometer software (Synerjy), set the grating mirror to be centred at 1550 nm (initially), the scanning time (per unit step size) to 0.3 s (don't forget to set the lock-in amplifier scanning time to 0.3 s too) and the entrance and exit slit widths to 0.3 mm respectively.
- 5. Conduct subsequent adjustments (with the mount screws) to obtain a maximized and steady signal. The adjustments need to be done on a very precise and minute scale so as to avoid deviating from the spot altogether.
- 6. Once a strong steady signal was obtained from the sample, select a range of wavelengths to scan upon. Scan in the 1.4  $\mu$ m to 1.65  $\mu$ m range to find out the full spectrum and verify the existence of modes. If there are no modes, find a different spot and try again.
- 7. When modes are found, pick one to concentrate on (usually the strongest or narrowest) and set the spectrometer grating to its peak wavelength. Use the XYZ screws in the sample stage to maximize the signal. Once the maximum signal is found, you are ready for further measurements.
- 8. If any experimental conditions are changed (temperature, laser power, etc.) it is necessary to re-maximize the signal at the peak center wavelength to ensure reproducibility of the measurements (this is

critically important for power dependent measurements of laser threshold).

# **Setting up the Cryostat**:

- Mount the cryostat chamber atop the xyz-stage and make sure it is securely attached.. Clean the cryostat cold finger, using IPA and wipe with a clean dry kimwipe.
- 2. Use an air spray with an attached nozzle to clean any dusts and particles inside the cryostat.
- 3. Clean the O-ring band sealing the chamber lid for containing vacuum, using IPA and apply vacuum grease.
- 4. Clean the see-through glass cover of the cryostat lid thoroughly.
- 5. Mount your sample inside using the vacuum grease is an adhesive.

# **Pumping and Cooling Down:**

- Attach the cryostat to a vacuum inducing turbo pump; clean the orings. Make sure all transfer lines are attached securely.
- 2. Pump the cryostat chamber for at least three hours (preferably overnight to achieve an effective measure of  $\sim 2$  e-6 mbar).
- 3. Connect a transfer line from the liquid Helium/Nitrogen tank to begin the cooling down procedure.
- 4. Slowly open the coolant transfer valve to let the coolant in (It takes a 5-10 minutes before the temperature starts dropping).
- 5. Continue pumping until the temperature is below 100 K and becomes stable at 82 K.
- 6. For sensitive measurements, the pump was turned off to avoid having any vibrations in the system due to the pumping motor.

# **Bibliography**

- [1] G. Moore, "Excerpts from A Conversation with Gordon Moore:

  Moore's Law," Interview by Intel Corporation, Intel Corporation

  Website, <a href="mailto:ftp://download">ftp://download</a>. intel. com/museum/Moores\_Law/Video
  Transcripts/Excepts\_A\_Conversation\_with\_Gordon\_Moore. pdf

  (accessed December 9, 2009), 2005.
- [2] R. H. Havemann and J. A. Hutchby, "High-performance interconnects:

  An integration overview," *Proceedings of the IEEE*, vol. 89, pp. 586-601, 2001.
- [3] D. A. B. Miller, "Optical interconnects to silicon," *Selected Topics in Quantum Electronics, IEEE Journal of*, vol. 6, pp. 1312-1317, 2000.
- [4] J. Yang, P. Bhattacharya, Z. Mi, G. Qin, and Z. Ma, "Quantum dot lasers and integrated optoelectronics on silicon platform Invited Paper," *Chinese Optics Letters*, vol. 6, pp. 727-731, 2008.
- [5] L. Liu. 31 May 2012). Available:

  <a href="http://photonics.intec.ugent.be/research/topics.asp?ID=82">http://photonics.intec.ugent.be/research/topics.asp?ID=82</a>
- [6] S. Chakravarty, P. Bhattacharya, and Z. Mi, "Electrically injected quantum-dot photonic crystal microcavity light-emitting arrays with air-bridge contacts," *Photonics Technology Letters, IEEE*, vol. 18, pp. 2665-2667, 2006.
- [7] V. Y. Prinz, S. V. Golod, V. I. Mashanov, and A. K. Gutakovsky, "Free-standing conductive GeSi/Si helical microcoils, micro-and nanotubes," 2000, pp. 203-206.
- [8] V. Y. Prinz, V. A. Seleznev, A. K. Gutakovsky, A. V. Chehovskiy, V.V. Preobrazhenskii, M. A. Putyato, and T. A. Gavrilova, "Free-

- standing and overgrown InGaAs/GaAs nanotubes, nanohelices and their arrays," *Physica E: Low-dimensional Systems and Nanostructures*, vol. 6, pp. 828-831, 2000.
- [9] Q. Song, H. Cao, S. T. Ho, and G. S. Solomon, "Near-IR subwavelength microdisk lasers," *Applied Physics Letters*, vol. 94, p. 061109, 2009.
- [10] L. W. Sung and H. H. Lin, "Highly strained 1.24-μm InGaAs/GaAs quantum-well lasers," *Applied Physics Letters*, vol. 83, pp. 1107-1109, 2003.
- [11] P. R. Berger, K. Chang, P. Bhattacharya, J. Singh, and K. K. Bajaj, "Role of strain and growth conditions on the growth front profile of InxGa1-xAs on GaAs during the pseudomorphic growth regime," *Applied Physics Letters*, vol. 53, pp. 684-686, 1988.
- [12] L. Goldstein, F. Glas, J. Y. Marzin, M. N. Charasse, and G. Le Roux, "Growth by molecular beam epitaxy and characterization of InAs/GaAs strained-layer superlattices," *Applied Physics Letters*, vol. 47, pp. 1099-1101, 1985.
- [13] R. A. Serway, C. J. Moses, and C. A. Moyer, *Modern physics*:

  Brooks/Cole Pub Co, 2005.
- [14] L.-W. Wang, "A New Model of Qauntum Dots: Rethinking the Electronics," *Research News: Berkley Lab*.
- [15] C. J. Murphy, "Peer Reviewed: Optical Sensing with Quantum Dots,"

  Analytical Chemistry, vol. 74, pp. 520-526, 2002.
- [16] R. Sauleau, "Fabry–Perot Resonators," *Encyclopedia of RF and Microwave Engineering*, 2005.

- [17] Free Spectral Range. Wikipedia (29 May 2012). Available: http://en.wikipedia.org/wiki/Free\_spectral\_range
- [18] P. Bhattacharya, "Semiconductor Optoelectronic Devices," ed Prentice Hall, 1994, pp. 261-263.
- [19] 29 May 2012). Q Factor. Encyclopedia of Laser Physics and Technology. Available: http://www.rp-photonics.com/q\_factor.html
- [20] Q Factor. Wikipedia. Available: <a href="http://en.wikipedia.org/wiki/Q\_factor">http://en.wikipedia.org/wiki/Q\_factor</a>
- [21] P. Bhattacharya, "Lasers: Structures and Properties," in *Semiconductor Optoelectronic Devices*, ed: Prentice Hall, 1994, pp. 275-277.
- [22] K. J. Vahala, "Optical Microcavities," *Nature*, vol. 424, pp. 841-843, 2003.
- [23] E.M.Purcell, "Proceedings of the American Physical Society," *Physical Review*, vol. 69, pp. 674-674, 1946.
- [24] A. Kavokin, "Weak Coupling Microcavities," in *Microcavities*, ed New York, United States: Oxford University Press, 2007, pp. 221-223.
- [25] X. Li, "Strain induced semiconductor nanotubes: from formation process to device applications," *Journal of Physics D: Applied Physics*, vol. 41, p. 193001, 2008.
- [26] R. Ito and S. Okazaki, "Pushing the limits of lithography," *Nature*, vol. 406, pp. 1027-1031, 2000.
- [27] K. Ariga, J. P. Hill, M. V. Lee, A. Vinu, R. Charvet, and S. Acharya, "Challenges and breakthroughs in recent research on self-assembly," *Science and Technology of Advanced Materials*, vol. 9, p. 014109, 2008.

- [28] V. Y. Prinz, "A new concept in fabricating building blocks for nanoelectronic and nanomechanic devices," *Microelectronic engineering*, vol. 69, pp. 466-475, 2003.
- [29] C. Deneke, C. Müller, N. Y. Jin-Phillipp, and O. G. Schmidt, "Diameter scalability of rolled-up In (Ga) As/GaAs nanotubes," Semiconductor science and technology, vol. 17, p. 1278, 2002.
- [30] K. Dietrich, C. Strelow, C. Schliehe, C. Heyn, A. Stemmann, S. Schwaiger, S. Mendach, A. Mews, H. Weller, and D. Heitmann, "Optical modes excited by evanescent-wave-coupled PbS nanocrystals in semiconductor microtube bottle resonators," *Nano Letters*, vol. 10, pp. 627-631, 2010.
- [31] F. Li and Z. Mi, "Optically pumped rolled-up InGaAs/GaAs quantum dot microtube lasers," *Optics Express*, vol. 17, pp. 19933-19939, 2009.
- [32] P. Poole, K. Kaminska, P. Barrios, Z. Lu, and J. Liu, "Growth of InAs/InP-based quantum dots for 1.55 [mu] m laser applications," *Journal of Crystal Growth*, vol. 311, pp. 1482-1486, 2009.
- [33] T. Kipp, H. Welsch, C. Strelow, C. Heyn, and D. Heitmann, "Optical modes in semiconductor microtube ring resonators," *Physical review letters*, vol. 96, p. 77403, 2006.
- [34] S. V. Golod, V. Y. Prinz, V. I. Mashanov, and A. K. Gutakovsky, "Fabrication of conducting GeSi/Si micro-and nanotubes and helical microcoils," *Semiconductor science and technology*, vol. 16, p. 181, 2001.

- [35] O. Schumacher, S. Mendach, H. Welsch, A. Schramm, C. Heyn, and W. Hansen, "Lithographically defined metal-semiconductor-hybrid nanoscrolls," *Applied Physics Letters*, vol. 86, p. 143109, 2005.
- [36] R. Songmuang, A. Rastelli, S. Mendach, and O. G. Schmidt, "SiOx/Si radial superlattices and microtube optical ring resonators," *Applied Physics Letters*, vol. 90, pp. 091905-091905-3, 2007.
- [37] H. Saito, K. Nishi, and S. Sugou, "Influence of GaAs capping on the optical properties of InGaAs/GaAs surface quantum dots with 1.5 μm emission," *Applied Physics Letters*, vol. 73, p. 2742, 1998.
- [38] P. Bianucci, Z. Tian, V. Veerasubramanian, A. G. Kirk, D. V. Plant, P. J. Poole, and Z. Mi, "Self-organized quantum-dot semiconductor microtube resonators and their integration on silicon photonics platforms," in *Information Photonics (IP), 2011 ICO International Conference on*, 2011, pp. 1-2.
- [39] C. Strelow, H. Rehberg, C. M. Schultz, H. Welsch, C. Heyn, D. Heitmann, and T. Kipp, "Optical microcavities formed by semiconductor microtubes using a bottlelike geometry," *Physical review letters*, vol. 101, p. 127403, 2008.
- [40] J. R. Rodriguez, J. G. C. Veinot, P. Bianucci, and A. Meldrum, "Whispering gallery modes in hollow cylindrical microcavities containing silicon nanocrystals," *Applied Physics Letters*, vol. 92, pp. 131119-131119-3, 2008.
- [41] J. Heo, "Nanoscale Lasers with Optical Microcavities," Ph.D, Electrical Engineering, University of Michigan, 2011.

- [42] Z. Tian, V. Veerasubramanian, P. Bianucci, S. Mukherjee, Z. Mi, A. G. Kirk, and D. V. Plant, "Single rolled-up InGaAs/GaAs quantum dot microtubes integrated with silicon-on-insulator waveguides," *Optics Express*, vol. 19, pp. 12164-12171, 2011.
- [43] A. S. Davydov, *Quantum Mechanics*. Oxford: Pergamon Press, 1995.
- [44] Y. P. Varshni, "Temperature dependence of the energy gap in semiconductors," *Physica*, vol. 34, pp. 149-154, 1967.
- [45] M. Wojdyr, "Fityk: a general-purpose peak fitting program," *Journal of Applied Crystallography*, vol. 43, pp. 1126-1128, 2010.
- [46] G. Bjork and Y. Yamamoto, "Analysis of semiconductor microcavity lasers using rate equations," *Quantum Electronics, IEEE Journal of*, vol. 27, pp. 2386-2396, 1991.
- [47] Z. Mi, P. Bianucci, F. Li, Z. Tian, V. Veerasubramanian, A. G. Kirk,
   D. V.Plant, and P. J. Poole, "Self-organized InAs quantum dot tube lasers and integrated optoelectronics on Si", Proc. SPIE 79431C, 2011.
- [48] 29 May 2012, Tube Lasers Prepare to Light Up Silicon Circuits.

  \*Compound Semiconductor\*. Available:

http://compoundsemiconductor.net/csc/features-

details/19498536/Tube-lasers-prepare-to-light-up-silicon-circuit.html